Article

Cell Reports

Mucus Architecture and Near-Surface Swimming Affect Distinct *Salmonella* Typhimurium Infection Patterns along the Murine Intestinal Tract

Graphical Abstract

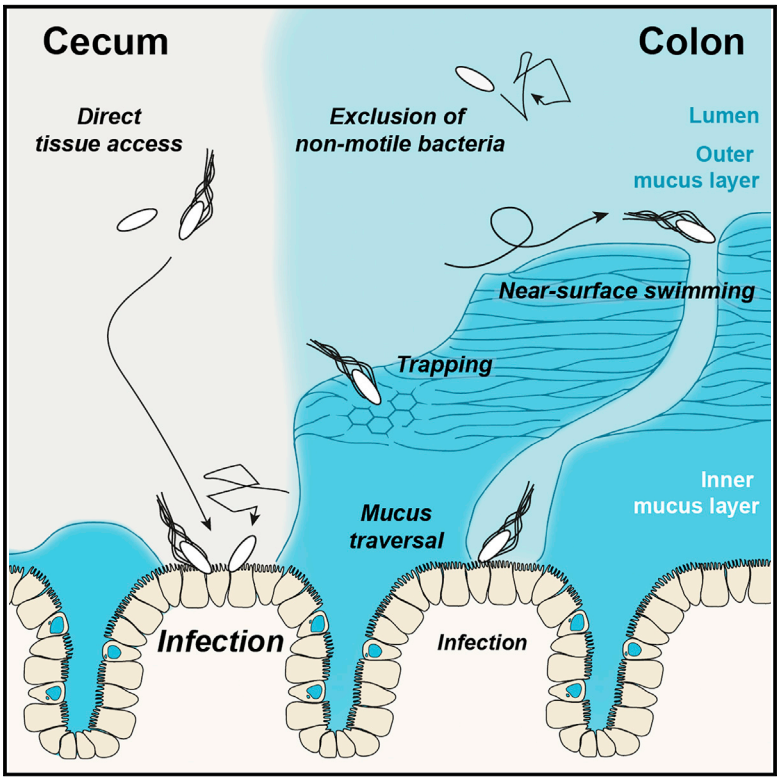

Highlights

- Live imaging of *Salmonella* near-surface swimming on mouse colon inner mucus layer
- Colon inner mucus layer traversal requires mucus breaches and flagellar propulsion
- The mouse cecum lacks a continuous mucus layer, leaving epithelium tips uncovered
- Exposed cecum epithelium tips are a hotspot for *Salmonella* infection

Authors

Markus Furter, Mikael E. Sellin, Gunnar C. Hansson, Wolf-Dietrich Hardt

Correspondence

hardt@micro.biol.ethz.ch

In Brief

Using live microscopy, Furter et al. describe how the enteropathogen *Salmonella* Typhimurium crosses the protective intestinal mucus layer of its murine host. Flagella-driven motility, the mucus architecture, and its distribution determine where the pathogen preferentially infects the gut epithelium.

Furter et al., 2019, Cell Reports *27*, 2665–2678
May 28, 2019
https://doi.org/10.1016/j.celrep.2019.04.106

CellPress

Cell Reports
Article

Mucus Architecture and Near-Surface Swimming Affect Distinct *Salmonella* Typhimurium Infection Patterns along the Murine Intestinal Tract

Markus Furter,[1] Mikael E. Sellin,[1,3] Gunnar C. Hansson,[2] and Wolf-Dietrich Hardt[1,4,*]
[1]Institute for Microbiology, ETH Zürich, 8093 Zürich, Switzerland
[2]Department of Medical Biochemistry, University of Gothenburg, 40530 Gothenburg, Sweden
[3]Present address: Science for Life Laboratory, Department of Medical Biochemistry and Microbiology, Uppsala University, 75123 Uppsala, Sweden
[4]Lead Contact
*Correspondence: hardt@micro.biol.ethz.ch
https://doi.org/10.1016/j.celrep.2019.04.106

SUMMARY

Mucus separates gut-luminal microbes from the tissue. It is unclear how pathogens like *Salmonella* Typhimurium (*S.*Tm) can overcome this obstacle. Using live microscopy, we monitored *S.*Tm interactions with native murine gut explants and studied how mucus affects the infection. A dense inner mucus layer covers the distal colon tissue, limiting direct tissue access. *S.*Tm performs near-surface swimming on this mucus layer, which allows probing for colon mucus heterogeneities, but can also entrap the bacterium in the dense inner colon mucus layer. In the cecum, dense mucus fills only the bottom of the intestinal crypts, leaving the epithelium between crypts unshielded and prone to access by motile and non-motile bacteria alike. This explains why the cecum is highly infection permissive and represents the primary site of *S.*Tm enterocolitis in the streptomycin mouse model. Our findings highlight the importance of mucus in intestinal defense and homeostasis.

INTRODUCTION

In the small intestine and the colon, a layer of mucus covers the gut epithelium and acts as a barrier, separating the microbes from the host tissue (Johansson et al., 2008; Ermund et al., 2013b). The main structural component of the mucus are the mucins, highly glycosylated and interconnected proteins that form a viscous hydrogel, shielding the epithelium against microorganisms. Antimicrobial peptides (AMPs) fortify the mucus barrier, and the zymogen ZG16 aggregates bacteria (Muniz et al., 2012; Bergström et al., 2016). Goblet cells constantly replenish the mucus, balancing losses from microbiota-mediated mucus degradation and from abrasion (Johansson, 2012). The distal colonic mucus can be divided into an outer layer, colonized by bacteria, and a mostly sterile inner layer (Li et al., 2015; Johansson et al., 2008). The colonic mucus layer thickness depends on the host species but also on the composition of the resident microbial community (Jakobsson et al., 2015). The small intestine features a different mucus architecture. Notably, the ileum shows an easily detachable, single mucus layer (Atuma et al., 2001; Ermund et al., 2013a). By contrast, less is known about the mucus of the cecum, a murine gut segment preferentially infected by *Salmonella enterica* subsp. *enterica* serovar Typhimurium (*S.*Tm) in the streptomycin mouse infection model.

The mucus is crucial for gut homeostasis. Mice lacking the structural mucin Muc2 develop spontaneous colitis in response to the resident microbiota (Van der Sluis et al., 2006; Petersson et al., 2011). Breaches of the mucus layer are observed in chronic inflammatory diseases such as ulcerative colitis (Swidsinski et al., 2005; Johansson et al., 2014), Crohn's disease (Schultsz et al., 1999), and Dextran sodium sulfate (DSS)-induced colitis models (Johansson et al., 2010, 2014; Bergstrom et al., 2010). The vicious cycle of inflammation and dysbiosis is characterized by disruption of the mucus structure and continuous hyper-stimulation of the immune system by the microbiota. Intestinal inflammation also originates from pathogens such as enterohemorrhagic or enteropathogenic *Escherichia coli* (EHEC or EPEC), *Citrobacter rodentium*, and *S.*Tm (Kaiser et al., 2012). They can assault the healthy mucosa and attach to or invade host epithelial cells that lie below the mucus layer. However, it remains unclear how such enteropathogenic bacteria can traverse the mucus to reach the epithelial surface.

The streptomycin mouse model allows deciphering the interplay between *S.*Tm and the host's gut mucosa (Barthel et al., 2003; Wotzka et al., 2017). The disease begins in the cecum within 8–12 h, when *S.*Tm reaches a density $\geq 10^8$ colony-forming units (CFU)/g luminal content (Barthel et al., 2003; Sellin et al., 2014; Ackermann et al., 2008). The rate of tissue invasion and disease progression is reduced in non-flagellated *S.*Tm mutants, indicating that active motility facilitates infection (Stecher et al., 2004). Tissue invasion triggers a rapid inflammatory response by 12 h postinfection. The cecal pathology includes an interferon-γ (IFNγ) -mediated loss of mucus-filled vacuoles from the goblet cells (Songhet et al., 2011; Zarepour et al., 2013). In the colon, the disease proceeds with slower kinetics, showing enteropathy after 1 day of infection. No signs of overt disease are observed in the absorptive mucosa of the small intestine,

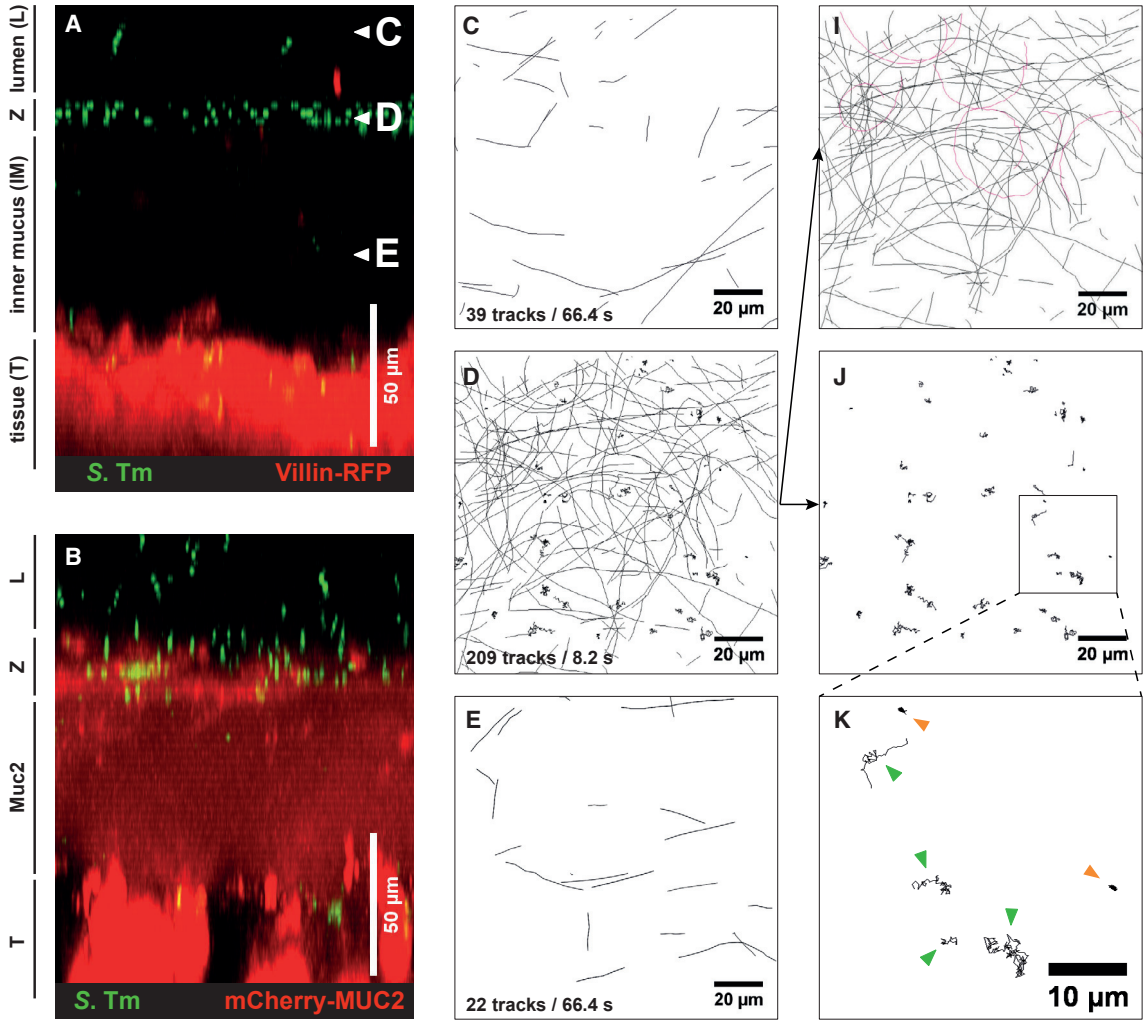

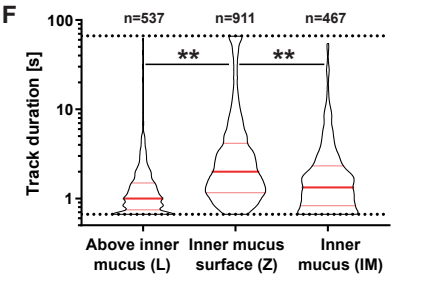

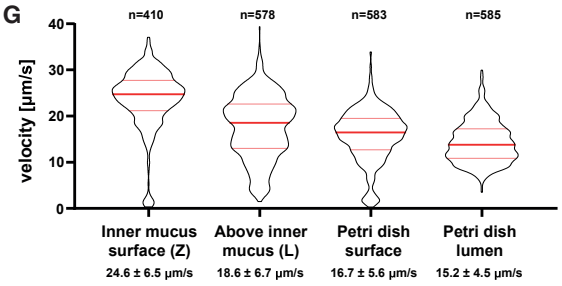

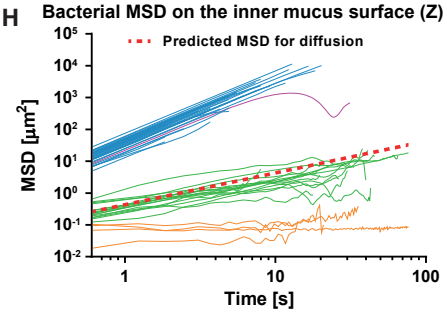

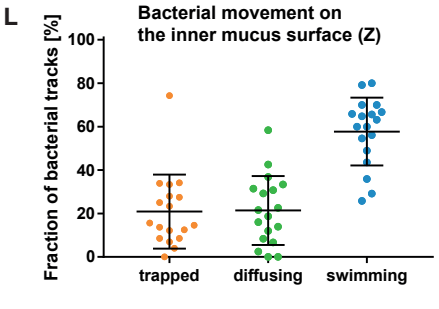

(legend on next page)

at least during the first 4 days of infection. It has remained elusive why disease kinetics and severity differ so substantially between the individual segments of the murine gut.

Here, we use live microscopy to study the protective functions of the host's mucus layer. This reveals striking differences in mucus distribution and architecture between the cecum and the colon, and establishes how this affects the infection process.

RESULTS

*S.*Tm Exhibits Near-Surface Swimming, Diffusion, and Entrapment on the Inner Colonic Mucus Layer

The interaction of *S.*Tm with the murine gut mucus was studied at the cellular level using live microscopy. Instead of synthesizing an artificial gel (Qi et al., 2017) or using porcine mucus (Celli et al., 2009; Constantino et al., 2016), we imaged constitutively GFP-expressing *S.*Tm (*S.*Tm^{GFP}, pM965) swimming on freshly excised distal colon tissue, including its native mucus layer. Initially, we used *villin-RFP* mice, which feature bright red fluorescent gut epithelial cells (Müller et al., 2012). For microscopy, the gut tissue was mounted, submerged in Krebs buffer, and imaged for <30 min to avoid tissue degradation.

Time-lapse imaging of distal colon tissue explant infections revealed a well-defined layer about 50–70 μm above the epithelium, where *S.*Tm^{GFP} accumulated (Figures 1A and 1D, labeled Z). Literature data report an inner colon mucus layer thickness of 50–100 μm, and that this layer prevents bacteria from reaching the tissue (Johansson et al., 2008). Also, fluorescent beads accumulate on the inner mucus layer when added onto explanted tissue (Gustafsson et al., 2012b). Thus, we suspected that *S.*Tm also accumulated on top of the inner colon mucus layer in our experiment (Figure 1A, labeled IM). To demonstrate that the space in between *S.*Tm^{GFP} and the RFP-labeled epithelium was indeed filled with mucus, we repeated the experiment with transgenic *RedMUC2*^{98trTg} mice that produce fluorescently labeled intestinal mucus (Birchenough et al., 2016). As expected, *S.*Tm accumulated at the mucus surface but was excluded from the bulk of the brightly fluorescent inner mucus layer (Figure 1B). The surface of the inner mucus layer has a sharp transition to the looser, outer mucus layer (Johansson et al., 2008). This loose structure covers the inner mucus layer and is penetrable for bacteria-sized beads, but not charcoal particles (Gustafsson et al., 2012a; Johansson et al., 2010, 2011). Our experiments did not specifically address the presence of this outer mucus layer. Thus, we refer to this zone above the inner mucus layer as lumen or loose mucus (labeled L).

To study the interaction of *S.*Tm with the mucus layer, we recorded confocal time-lapse movies in the lumen or loose mucus (Figures 1A and 1C, labeled L), at the surface (Z) of the inner mucus layer (Figures 1A and 1D), and within the inner mucus (Figures 1A and 1E, labeled IM). Bacteria were tracked with ImageJ (TrackMate; Tinevez et al., 2017). Above the inner mucus layer, most bacteria produced very short tracks and left the imaged Z section within 1.5 s (Figures 1C and 1F; Video S1). This is attributable to bacteria moving through the image plane in a vertical direction. In contrast, *S.*Tm showed a much higher density and longer tracks at the surface (Z) of the inner colonic mucus (Figures 1D and 1F; Video S2). Fewer *S.*Tm were observed within the inner mucus layer (Figures 1A–1F, labeled IM; Video S3). This is in line with the protective function of the colonic mucus. To analyze the swimming speed in more detail, we plotted the tracking data as mean squared displacement (MSD) of the bacterial cell over time. This revealed three classes of movement patterns on the surface (Z) of the colon's inner mucus layer (Figure 1H).

Most *S.*Tm cells were actively moving along the image plane (Figures 1H and 1I). A smaller fraction of these was moving on circular trajectories (Figure 1I, magenta tracks), which results in oscillating MSD curves (Figures 1H and S1A). This indicates near-surface swimming (NSS), a phenomenon that is typically observed when swimming bacteria encounter a smooth, solid surface (Lauga et al., 2006; Misselwitz et al., 2012) (Figure S1B). Strikingly, NSS can be observed on the inner mucus layer surface (Z), which is a soft biological material. We measured the speed of the actively swimming *S.*Tm population on the inner mucus layer (Z; 24.6 ± 6.5 μm/s) of the distal colon and in areas >20 μm above (L; 18.6 ± 6.7 μm/s). As a control experiment, we measured *S.*Tm swimming in Petri dishes, without murine tissue. Compared with the distal colon tissue, *S.*Tm moved slightly slower across the surface (16.7 ± 5.6 μm/s) and in the

Figure 1. Tracking of *S.*Tm on the Colon Mucus Surface Reveals Three Different Swimming Patterns

(A and B) Distal colon tissue from untreated mice (*villin-RFP*, A, or *RedMUC2*^{98trTg}, B) was infected with *S.*Tm^{GFP}, and we recorded z stacks as well as time-lapse series (six frames/second).

(C–E) *S.*Tm tracks from image planes above the inner mucus (C), on the inner mucus surface (D), or below the mucus surface (E) in the image stack (A) are shown. Numbers indicate the tracks shown and the time interval in which they originated.

(F) Quantification of the *S.*Tm track duration. Each dot represents one bacterial track. Red bars indicate median and quartiles. Data were pooled from two independent experiments. Statistics: non-parametric one-way ANOVA. **$p < 0.01$.

(G) Bacterial swimming speed. Petri dish represents control. Red bars indicate the median and the quartiles. A non-parametric one-way ANOVA showed significant differences between all groups.

(H) Mean squared displacement (MSD) calculated for 50 random *S.*Tm tracks from (D). Blue represents actively swimming; green represents diffusing; orange represents trapped *S.*Tm. The red dotted line indicates theoretical behavior of a 2-μm particle diffusing in water.

(I–K) For visibility reasons, the tracks in (D) were separated in two images based on their MSD.

(I) Tracks of actively swimming *S.*Tm. Magenta represents circular tracks (NSS).

(J and K) Slower tracks are shown in (J) and were magnified for better visibility (K). Green arrows indicate diffusing, and orange arrows represent trapped bacteria.

(L) Fraction of trapped, diffusing, and swimming *S.*Tm, as assessed manually based on optical appearance of the tracks. Data are from four independent experiments. Each data point represents one image series. Bars indicate mean ± SD.

IM, inner mucus layer; L, lumen or loose mucus; T, epithelial tissue; Z, zone of *S.*Tm accumulation.

See also Figure S1 and Videos S1, S2, and S3.

bulk liquid (15.2 ± 4.5 μm/s) of the Petri dish (Figure 1G). The reduced speed might be attributable to different drag or frictional forces imposed by the dish plastic versus the mucus surface. Nevertheless, our data indicate that *S.*Tm motility was certainly not slowed down, neither during near-surface swimming on the inner colonic mucus layer nor in the lumen or looser mucus layer above.

The second type of motility observed on the colonic mucus surface was *S.*Tm diffusion by Brownian motion (Figures 1D, 1J, and 1K). Brownian motion was verified by plotting the MSD and calculating the diffusion coefficient of the bacterial tracks (0.233 ± 0.004 $\mu m^2/s$) (Figure 1H, green), which is close to the value calculated for a spherical particle with 2-μm diameter in water (0.2143 $\mu m^2/s$) (Figure 1H, red line). The expression of flagella is costly for *S.*Tm and regulated in a bi-stable manner (Freed et al., 2008; Cummings et al., 2006). Depending on nutrient availability, the fraction of the flagellated *S.*Tm population varies between 0% and 90% (Koirala et al., 2014). This co-existence of flagellated and non-flagellated subpopulations explains the occurrence of both swimming (blue) and diffusing (green) *S.*Tm cells in our assay (Figure 1H).

The third fraction of *S.*Tm cells was completely immobile (Figures 1D, 1J, and 1K). These *S.*Tm cells formed a distinct class in the MSD plot (Figure 1I) and in the magnification of the bacterial tracks (Figure 1K, orange). The immobilized bacteria were located at the inner colon mucus surface (Figures 1C–1E). Few such cells were found below the Z layer and none in the lumen or loose mucus layer. 21% of the *S.*Tm at the inner mucus surface were in this trapped state, 57% were actively swimming, and 22% were diffusing (Figure 1L). In conclusion, *S.*Tm interacts with the surface of the inner mucus of the colon, and the interaction results in three distinct motility phenotypes: swimming, diffusion, and entrapment.

Trapping of *S.*Tm in the Colonic Mucus Layer Depends on Flagellar Motility

Entrapment of bacteria by the mucus surface could be a potent mechanism to protect the tissue from bacterial onslaught. Trapping in the mucus could depend on several mechanisms. One is that the mucus acts as a filter, preventing *S.*Tm from penetrating the pores of the mucus meshwork (Johansson et al., 2014). Alternatively, bacterial flagella could adhere to mucin glycans (Haiko and Westerlund-Wikström, 2013). We thus analyzed *S.*Tm$^{\Delta fliGHI}$ (Stecher et al., 2004), a mutant strain that lacks structural components for flagellar assembly. *S.*Tm$^{\Delta fliGHI}$ accumulated at the mucus surface (Figure 2A). As expected, *S.*Tm$^{\Delta fliGHI}$ did not engage in NSS and moved by diffusion alone (Figures 2B–2D; Video S4). Strikingly, we found hardly any trapped bacteria at the mucus surface of *S.*Tm$^{\Delta fliGHI}$-infected tissue (Figures 2D and 2E). Moreover, *S.*Tm$^{\Delta fliGHI}$ was virtually absent from the inner mucus layer (Figures 2A and 2I; see STAR Methods). 2.1% ± 2.1% of the wild-type (WT) *S.*Tm reached the colon epithelium, whereas 76.4% ± 12.6% did not manage to get below the mucus surface within the 25 min of our experiment (Figures 2F–2H). By contrast, none of the *S.*Tm$^{\Delta fliGHI}$ cells analyzed reached the colon epithelium (Figure 2I). We conclude that the colonic inner mucus is nearly impassable for non-motile *S.*Tm mutants, and that flagella are important for trapping of *S.*Tm in the mucin meshwork of the inner mucus layer.

To decipher the role of molecular binding of flagellar proteins in *S.*Tm entrapment, we used *S.*Tm$^{\Delta motA}$. This strain lacks the stator of the flagellar motor complex, leading to paralysis of the otherwise functional flagella (Ishihara et al., 1981). Similar to *S.*Tm$^{\Delta fliGHI}$, *S.*Tm$^{\Delta motA}$ did not swim actively but still reached the mucus surface by diffusion (Figure S2A). Again, no trapping of *S.*Tm$^{\Delta motA}$ was observed (Figures S2B–S2E). Thus, active motility rather than binding of flagellar proteins leads to entrapment of *S.*Tm at the inner mucus layer surface.

*S.*Tm Swimming Motility Can Permit Probing for Mucus Heterogeneities

To further assess the role of flagella in mucus penetration, we infected explanted tissue from the distal colon of *villin-RFP* mice with a 1:1 mix of *S.*Tm$^{\Delta fliGHI}$ and WT *S.*Tm expressing green or red fluorescent reporters, respectively. Both strains accumulated on the inner mucus surface (Figure 3A). However, the WT strain was on average residing 11.2 ± 10.5 μm closer to the tissue than *S.*Tm$^{\Delta fliGHI}$ (Figure 3B). We observed distinct areas of the mucus surface from which *S.*Tm$^{\Delta fliGHI}$ was excluded, as well as areas containing mostly trapped WT *S.*Tm (Figures 3C and 3D; Video S5). Closer inspection revealed that the trapped WT bacteria were located deeper within the mucus layer and closer to the tissue than the diffusing *S.*Tm (Figures 3E and 3F). This implied that *S.*Tm penetrates some part of the colonic mucus, based on its motility.

The proximal colon features major transverse folds, which allow time-lapse imaging of the mucus layer in a vertical direction. We have thus explanted proximal colon tissue from *villin-RFP* mice to study *S.*Tm-mucus interactions in real time (Figure 4A; Video S6). Again, most *S.*Tm cells accumulated in the Z-layer, and many of these engaged in NSS, diffused, or became trapped, whereas a small fraction traversed the inner mucus layer. *S.*Tm swims slower during this traversal of the proximal colon mucus layer than in the colonic lumen or on the mucus surface (Figure 4B; also compare with Figure 1G), suggesting that *S.*Tm experiences resistance or drag while swimming through permeable sites of the proximal colon mucus layer. Moreover, the bacteria crossed the mucus at distinct sites (Figure 4A). This was further addressed in proof-of-principle experiments on colon tissue explants from *RedMUC2*^{98trTg} mice (Birchenough et al., 2016). These mice feature a mixture of mouse Muc2 and mCherry-human MUC2, and show an aberrant inner mucus architecture (C. Wising, F. Svensson, L. Arike, J.K. Gustafsson, A. Ermund, A.M. Rodriguez-Pineiro, A. Schütte, G.M.H. Birchenough, F.H. Sterky, M.E.V. Johansson, G.C.H., unpublished data). The bacterial tracking data from these *RedMUC2*^{98trTg} mice further support that heterogeneous mucus structures allow site-specific passage of motile *S.*Tm (Figure S3). Please note that the interaction of *S.*Tm with this mCherry-MUC2 mucus does not reflect the natural interaction with the inner mucus of the distal colon. Previous studies report that the murine proximal colon mucus is heterogeneous and thereby permits local contact of the microbiota with the epithelium (Ermund et al., 2013b; Kamphuis et al., 2017). Mucus heterogeneities thus provide a plausible explanation for the observed mucus

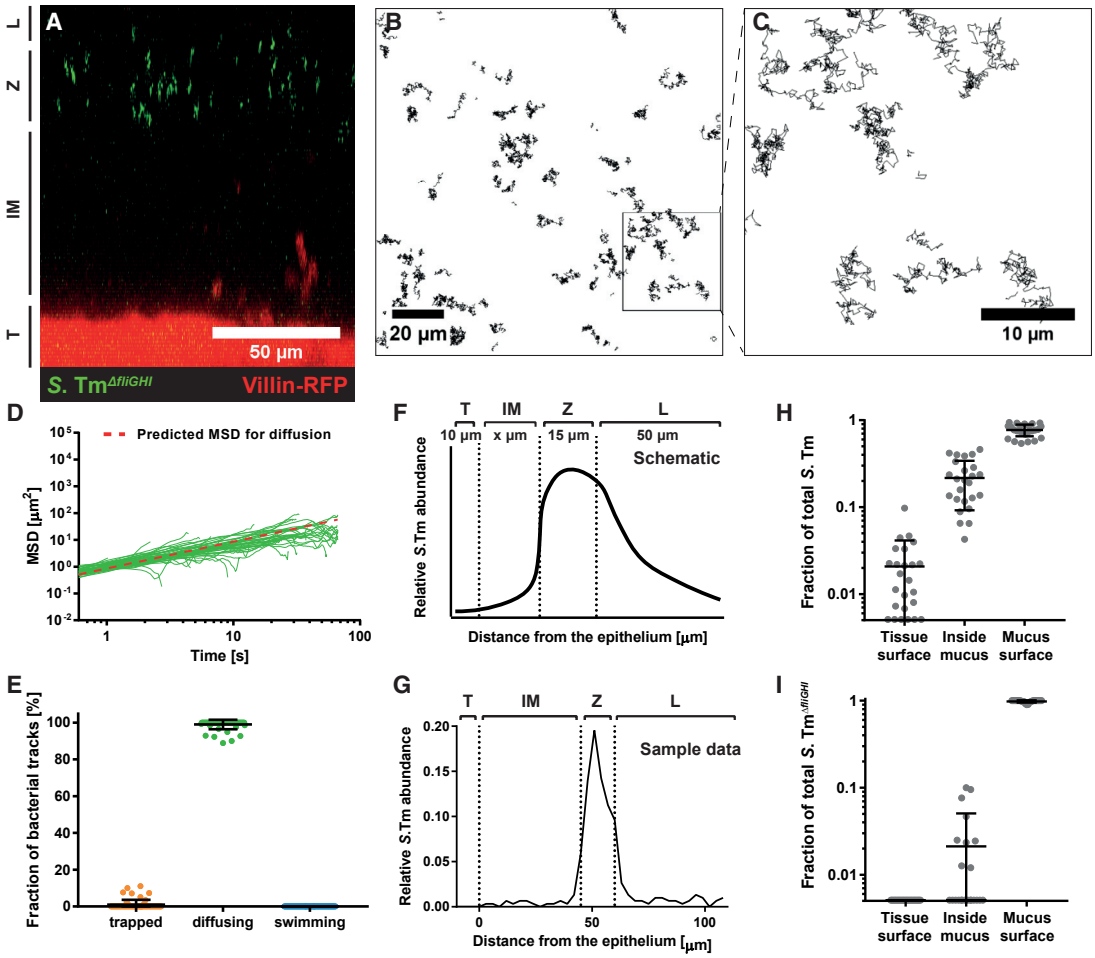

Figure 2. Colonic Mucus Holds Back More Than 75% of *S.*Tm, and Motility Is Required to Pass the Mucus

Distal colon tissue samples were excised from untreated *villin-RFP* mice and mounted on a Petri dish. After mounting, green fluorescent *S.*Tm$^{\Delta fliGHI}$ were added onto the tissue, and confocal image stacks were acquired.

(A) Side view of a representative z stack after addition of *S.*Tm$^{\Delta fliGHI}$. The image is labeled as in Figure 1.

(B) Time-lapse microscopy of *S.*Tm$^{\Delta fliGHI}$ was performed at the surface of the inner mucus layer to track bacterial motion. The bacterial tracks are shown in black.

(C) Magnification of the area marked in (B).

(D) MSD calculated from 50 random *S.*Tm$^{\Delta fliGHI}$ tracks at the colon mucus surface. The plot is color coded for the motility phenotype of each track as in Figure 1.

(E) Trapped, diffusing, and swimming *S.*Tm were quantified manually based on optical appearance of the tracks. Shown is the mean ± SD of three independent experiments. Each data point represents one image series.

(F and G) The distribution of *S.*Tm in the image stacks was assessed by automatic image analysis. Shown is a schematic drawing (F) and data from one representative image (G) of the *S.*Tm abundance with respect to the distance from the colon tissue. The images were split into the four parts: tissue surface (T), inner mucus layer (IM), lumen or loose mucus (L), and inner mucus surface (Z), defined as a range of 15 µm from the lower boundary of *S.*Tm accumulation.

(H and I) Estimation of the protective effect of the mucus. Plotted in $\log_{10}$ scale is the fraction of *S.*Tm (H) and *S.*Tm$^{\Delta fliGHI}$ (I) that was located at the tissue surface (T) or inside the mucus (IM) and on the mucus surface (Z), respectively. Bars indicate the mean ± SD of two independent experiments with two mice each. Each dot represents one image series.

See also Figure S2 and Video S4.

layer traversal (Figures 4A and 4B). NSS on the mucus layer could even enhance the chance of *S.*Tm to encounter and exploit such mucus heterogeneities in the colon.

The Murine Cecal Mucus Layer Has Large Gaps and Allows Epithelial Access, Even for Non-motile *S.*Tm

Different mucus architectures are well documented for the small intestine and the distal colon (Atuma et al., 2001; Johansson et al., 2008). Small intestinal mucus is not attached to the epithelium and is more penetrable for microorganisms and bacteria-sized beads than the distal colon. Furthermore, the properties of the inner mucus layer change along the colon in mice (Ermund et al., 2013a). However, less is known about the mucus architecture of the murine cecum. This is of particular interest because this site shows the earliest signs of pathology in the streptomycin mouse model for *S.*Tm enterocolitis (Kaiser et al., 2012; Barthel et al., 2003). We thus repeated our live-microscopy experiments and compared tissues from the colon, small intestine, and cecum.

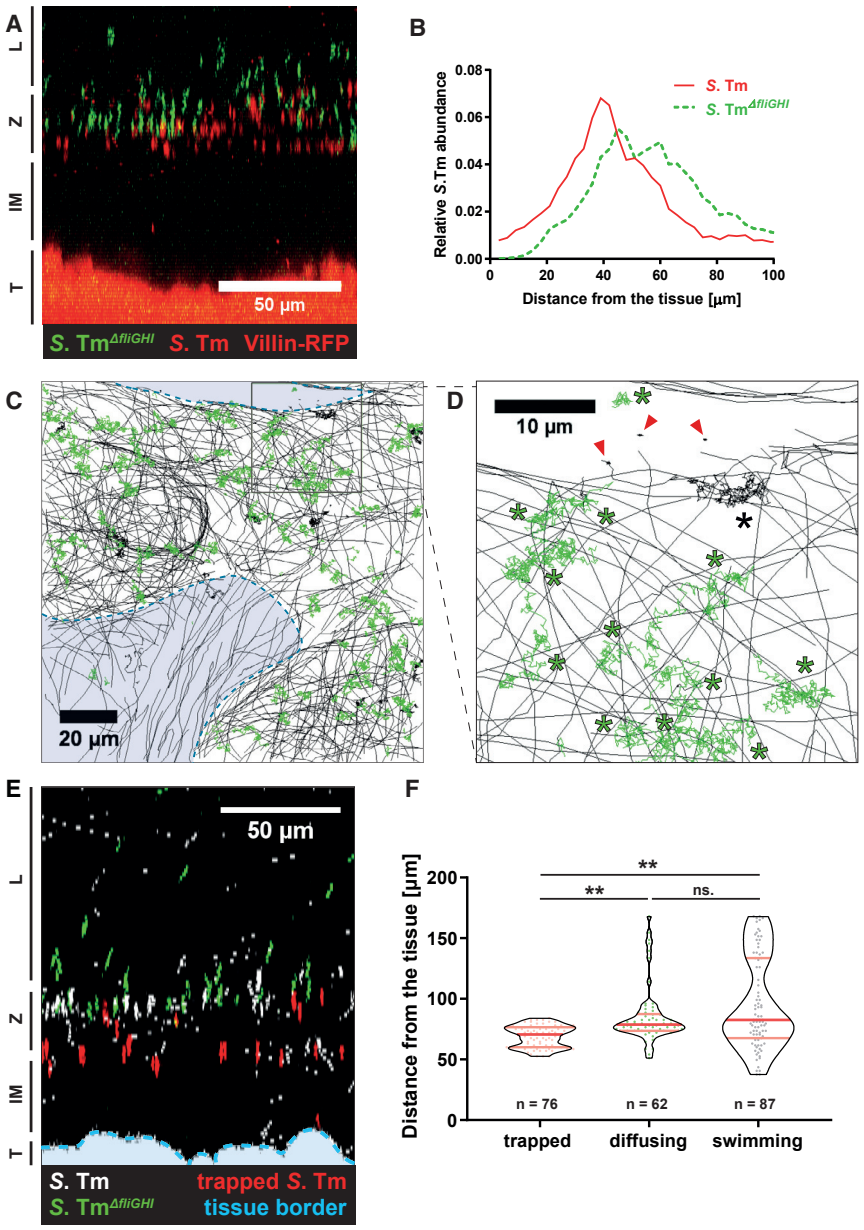

Figure 3. Motile and Trapped *S.*Tm Are Located Deeper in the Mucus Layer

Distal colon tissue samples were excised from untreated *villin-RFP* mice and mounted on a Petri dish. After mounting, green fluorescent *S.*Tm$^{\Delta fliGHI}$ and red fluorescent WT *S.*Tm were added as a 1:1 mixture onto the tissue.

(A) Side view of a confocal z stack after adding the bacterial mixture. The image is labeled as in Figure 1.

(B) Distribution of *S.*Tm$^{\Delta fliGHI}$ and WT *S.*Tm, measured with automated image analysis. Plotted is the abundance of each *S.*Tm population with respect to the distance from the epithelium. The graph indicates the mean distribution from four mice in two independent experiments.

(C) Time-lapse microscopy tracks of *S.*Tm$^{\Delta fliGHI}$ (green) and WT *S.*Tm (black) on the colon mucus surface. The areas marked in blue lie below the surface of the inner mucus and are less accessible for *S.*Tm$^{\Delta fliGHI}$. See also Video S5.

(D) Magnification of the area marked in (C). Diffusing bacteria are labeled with an asterisk, whereas trapped bacteria are marked with a red arrowhead.

(E) Side view of a confocal z stack from *villin*-RFP distal colon tissue after adding a 1:1 mixture of *S.*Tm$^{\Delta fliGHI}$ (green) and WT *S.*Tm (white). Trapped WT *S.*Tm were highlighted in red. The tissue border is marked with a blue dotted line.

(F) Quantification of the bacterial motion pattern with respect to the distance from the epithelium. Each dot represents one bacterium. Red lines delineate the median and quartiles. Statistics: non-parametric one-way ANOVA comparing the different groups. **p < 0.01. ns., not significant.

In the small intestine of *villin-RFP* mice, some *S.*Tm reached the space between the villi, but the bulk of the bacteria accumulated above the tips of the villi. The distance between the zone of *S.*Tm accumulation and the tip of the villi was variable and ranged between 5 and 30 µm (peak at 17.5 ± 2.1 µm; Figures 5A and 5B, green curve). In the distal colon, this distance was less variable, and *S.*Tm was typically located 50.5 ± 0.5 µm above the epithelium (Figures 5A and 5B, red curve). By contrast, *S.*Tm accumulated directly on the cecal epithelium surface without any additional zones of *S.*Tm accumulation distant from the tissue (Figures 5A and 5B, blue curve; Figure S4A). Many *S.*Tm were swimming along the epithelial surface with a speed of 18.1 ± 5.2 µm/s or were trapped directly on the epithelium (Figures S4B–S4E; Video S7). These trapped bacteria could either be bound to the host cell glycocalyx (Li et al., 2019) or irreversibly docked to the host cell via their type III secretion system 1, which is an essential step in host cell invasion (Misselwitz et al., 2011a, 2011b, 2012; Lara-Tejero and Galán, 2009). The fraction of *S.*Tm that reached the tissue surface (i.e., located directly on the tissue surface and trapped) was significantly higher in the cecum compared with colon or small intestine tissue explants (Figure 5C). Using these parameters for analysis, we found that 24.5% ± 10.6% of *S.*Tm in the cecum reach the tissue surface, whereas the small intestine (9.6% ± 9.6%) and colon (4.6% ± 5.3%) permit less epithelial access.

One reason for the pronounced accessibility of the cecal epithelium could be a thinner or discontinuous cecal mucus layer. To visualize the mucus, we compared *RedMUC2*^{98trTg} mouse tissue explants from the small intestine, colon, and cecum. As described above, although these mice produce a heterogeneous, aberrant inner mucus layer in the distal colon, they allow the direct visualization of the mucus (Figure S3) (C. Wising, F. Svensson, L. Arike, J.K. Gustafsson, A. Ermund, A.M. Rodriguez-Pineiro, A. Schütte, G.M.H. Birchenough, F.H. Sterky, M.E.V. Johansson, G.C.H., unpublished data). Fluorescein isothiocyanate

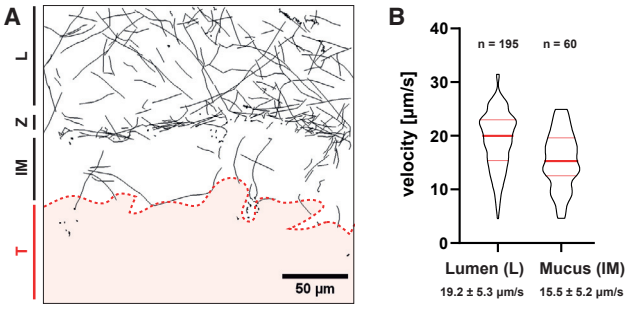

Figure 4. *S.*Tm Traverse the Mucus in Distinct Sites

(A) Time-lapse microscopy was performed perpendicular to the mucus layer at a fold of the proximal colon tissue of *villin-RFP* mice to track bacterial motion. Bacterial tracks are shown in black. The red area indicates the colon tissue. Area Z delineates the zone of bacterial accumulation atop the mucus layer and the lumen or loose mucus (L). See also Video S6.

(B) Quantification of the bacterial swimming speed. The velocity of actively swimming *S.*Tm was quantified in the lumen (L) and inner mucus (IM) of the explanted proximal colon tissue shown in (A). The swimming speed was compared with the data shown in Figure 1G using a non-parametric one-way ANOVA. Luminal *S.*Tm swimming speeds did not differ between experiments ($p > 0.05$). *S.*Tm swimming speed within the mucus was significantly lower ($p < 0.01$) than the speed in the lumen or on the mucus surface. Red bars indicate the median and quartiles.

See also Figure S3.

(FITC)-coated beads sedimented onto the distal colon mucus surface by gravity (Figure 5D). Mucus in the small intestine was less fluorescent and more permeable to fluorescent beads. This is consistent with our observation that *S.*Tm accumulates 5–30 μm above the small intestinal villi, and that some bacteria could reach the space between the small intestinal villi (Figures 5A and 5B). By contrast with the colon, the fluorescent beads reached the tissue surface in the cecum (Figure 5D). In a second experiment, we added fluorescent *S.*Tm$^{\Delta fliGHI}$ to explanted small intestinal, cecal, and colonic tissue of *villin-RFP* mice, which form regular mucus. In line with the bead sedimentation experiments in *RedMUC2*^{98trTg} mice, the cecal tissue of *villin-RFP* mice was accessible for non-motile, diffusing *S.*Tm$^{\Delta fliGHI}$, which were in rare cases even trapped at the tissue surface (Figures S4F–S4I).

Finally, we examined methacarn-fixed tissue samples of untreated C57BL/6 mice that were stained with α-Muc2 antibodies (Johansson and Hansson, 2012). In line with the explant experiments, the cecum lacked a continuous, Muc2-positive mucus layer (Figure 5E). Muc2 clouds were predominantly found at the bottom of the cecal crypts and were mostly absent at the top of the crypts and on the cecal patch (Figures 5E and 5G). The latter site has a role in antigen sampling from the luminal content, similar to Peyer's patches, and is a major site of *S.*Tm infection (Hohmann et al., 1978; Carter and Collins, 1974). In line with this discontinuous morphology, the average thickness of the mucus layer was significantly thinner in the cecum compared with both small intestine and colon (Figure 5F). The mucus thickness measured in the methacarn-fixed tissues was overall lower than in the explant experiments, as expected by the shrinkage of the water-rich mucus during fixation.

There are multiple factors that cannot be taken into account using the explant imaging technique presented above. Intestinal explants fail to recapitulate peristalsis, interactions with the microbiota, and the hypoxic conditions encountered *in vivo*. We thus performed verifying experiments by intra-vital microscopy, where we injected *S.*Tm^{GFP} into the cecum of *villin-RFP* mice (Sellin et al., 2014; Müller et al., 2012). In line with the explant experiments, *S.*Tm could get into close contact with the cecal tissue surface (Figures 6A and 6B, upper right and lower left side; Video S8). Some bacteria were moving along the epithelial surface, but most moved passively with the bulk of the cecal content. Light-induced heating of the sample created a flux of the cecal content and prevented the acquisition of longer time-lapse movies (Figure S5; Video S9). To circumvent the injection of *S.*Tm, we gavaged *villin-RFP* mice orally with FITC-coated latex beads and imaged the cecum 4 h after gavage by intra-vital microscopy (Figure 6C). Similar to the injected *S.*Tm, the beads got into close contact with the epithelial surface of the cecum (Figure 6D). The strong fluorescent signal of the beads even allowed imaging in the colon. There, the distance between beads and tissue was significantly larger than in the cecum, demonstrating the accessibility of the cecal tissue by *S.*Tm and fluorescent beads *in vivo*. These data verify the existence of architectural differences between cecal and colonic mucus *in vivo*.

Mucus Organization and Gut Luminal Pathogen Densities Limit Mucosal Invasion

Next, we assessed how mucus organization and pathogen densities might affect *S.*Tm tissue invasion rates. C57BL/6 mice were infected with *S.*Tm (pM975) and analyzed after 12 h, when gut lumen and tissue are fully colonized, but expulsion of infected epithelial cells and tissue inflammation have not become full-blown (Sellin et al., 2014; Hapfelmeier et al., 2005; Stecher et al., 2004).

The pathogen loads were low in the lumen of the proximal small intestine (median = 2.1×10^4 CFU/g) and increased toward the distal end of the small intestine (median = 4.1×10^6 CFU/g). It is, however, noteworthy that this pathogen density is not sufficient to trigger tissue pathology, at least within the first 12–48 h of infection (Barthel et al., 2003). Considerably higher pathogen densities were observed in the cecum and in the colonic lumen (median = $2.5–3.8 \times 10^9$ CFU/g; Figure 7A). Such densities are sufficient to cause disease in the cecum by 12 h postinfection (p.i.) and in the colon by 24–48 h p.i. (Barthel et al., 2003).

We observed very low intracellular pathogen loads in the proximal and medial small intestine (median < 1 per 20-μm section; Figure 7B). Intermediate tissue loads were observed in the distal small intestine and the proximal and distal colon (median = 7.5–29 per 20 μm-section). This is consistent with the absence of tissue pathology in the small intestine and the colon during the first 2 days of infection (Barthel et al., 2003). In the cecum, *S.*Tm was located mainly in epithelial cells, particularly in the exposed areas between intestinal crypts, which were not covered by mucus (Figure 7C). Pathogen tissue loads were about 10-fold higher in the cecum (median = 219 per 20-μm section) than in the colon (Figures 7B, 7D, and 7E). This factor is even higher *in vivo* than in our explant infection assay, where we found

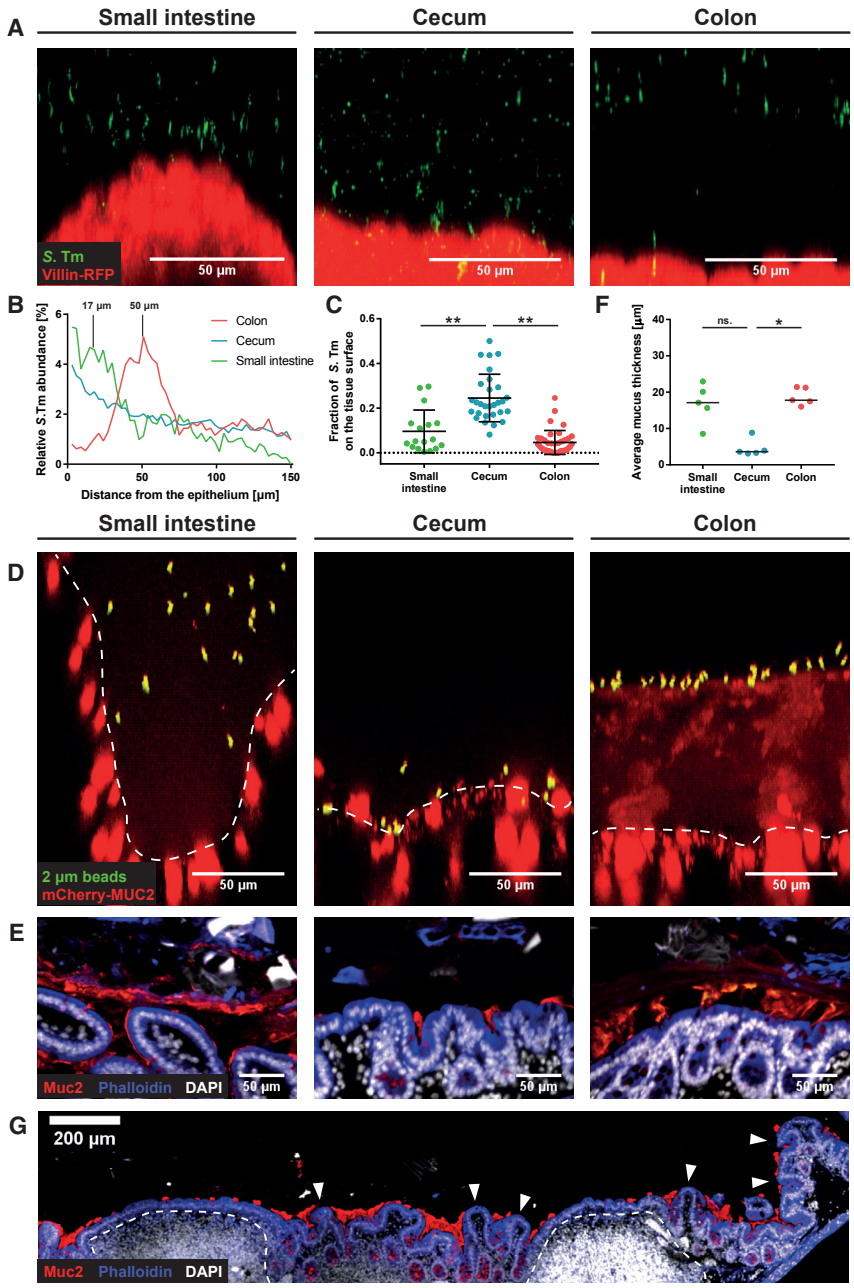

Figure 5. Cecum Mucus Covers the Crypts but Leaves the Tips of the Epithelium Exposed

(A–C) Gut tissue explants were infected and imaged as in Figure 1A.

(A) Side view of representative confocal z stacks.

(B) Distribution of *S.*Tm as measured by automated image analysis. Mean distribution across four independent experiments.

(C) Fraction of fluorescent *S.*Tm directly in contact with the tissue surface (versus total number of *S.*Tm within a distance of 100 µm from the epithelium). Bars indicate mean ± SD of four independent experiments. Each dot represents one image stack analyzed. Statistics: non-parametric one-way ANOVA comparing the different groups. $^{**}p < 0.01$.

(D) FITC-coated beads (2 µm) on gut tissue explants from untreated *RedMUC2*^{98trTg} mice. Dashed line indicates tissue border. The small intestinal image was taken at a site in between two villi, lacking the crypt.

(E–G) Methacarn-fixed gut tissue samples from untreated C57BL/6 mice were stained with α-Muc2 antibodies (red), phalloidin (blue), and DAPI (white). Shown are representative images (E) from the small intestine, cecum, and distal colon.

(F) Quantitative analysis of the mucus thickness in tissue sections from five mice as in (E). Each dot represents the measured average mucus thickness from one mouse. The black line delineates the median. Statistics: non-parametric one-way ANOVA comparing the different groups. $^{*}p < 0.05$; $^{**}p < 0.01$; ns., not significant.

(G) Overview image of the cecal patch from an untreated C57BL/6 mouse (as in E). Dashed line indicates lymphoid tissue; arrowheads indicate exposed epithelium.

See also Figure S4 and Video S7.

a ~5-fold difference (Figure 5C). The difference between the explant and the *in vivo* infection data could be explained by AMPs and phages stored in the mucus that confer antimicrobial activity (Antoni et al., 2013; Chromek et al., 2012; Meyer-Hoffert et al., 2008; Barr et al., 2013) or by pathogen-associated molecular pattern (PAMP)-triggered mucus expulsion (Birchenough et al., 2016). We can thus demonstrate that the net tissue invasion rate differs *in vivo* between the cecum and the colon.

Previous studies report an increase in mucus layer thickness and Muc2 expression at 3 and 7 days p.i. (Zarepour et al., 2013). This suggested that our measured infection rates could be affected by dynamic changes in the mucus architecture. However, mucus thickness did not change significantly during the first 12 h of infection in any segment of the gut or upon streptomycin pretreatment (compare Figures 7H and 7I with Figure 5F). *S.*Tm was located at the tissue surface in the cecum, whereas most *S.*Tm cells were separated from the colon tissue by mucus (Figures 7F and 7G). Hence, the high luminal pathogen densities and the lack of a continuous, protective mucus layer make the cecum the initial site of infection in mice.

DISCUSSION

The intestinal mucus is essential for gut homeostasis, separating the gut tissue from the microbiota and pathogens (Johansson et al., 2008; Ermund et al., 2013a). Here, we used *S.*Tm to investigate interactions between motile, pathogenic bacteria and the murine mucus. In the colon, a thick inner mucus layer elicits three distinct types of *S.*Tm motility behavior and reduces the infection efficiency by about 5- to 10-fold. We

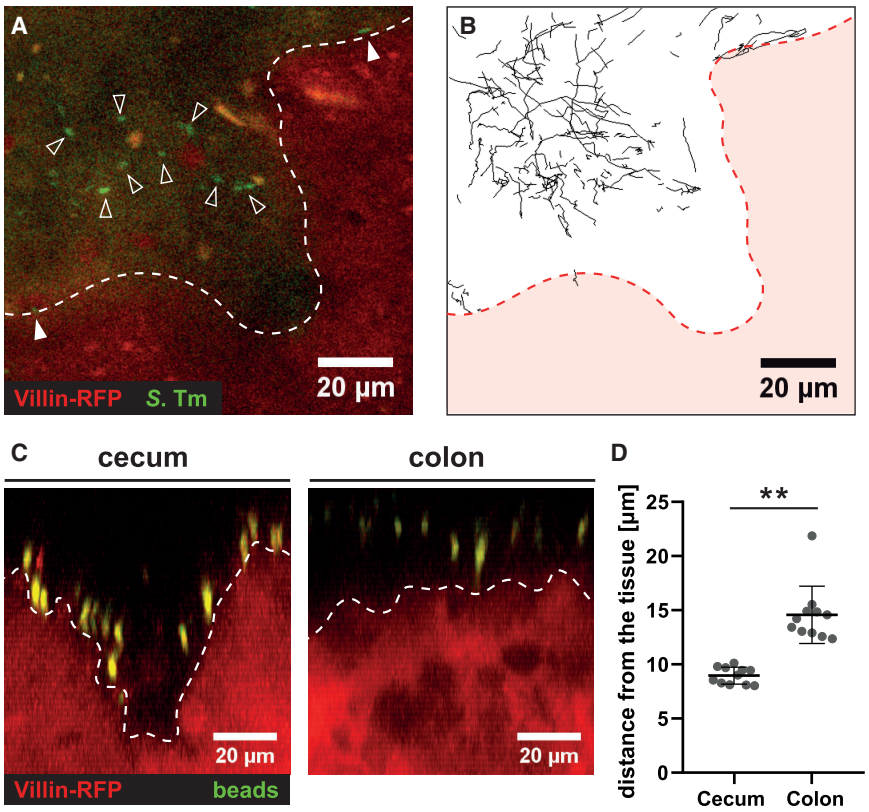

Figure 6. *S.*Tm^{GFP} and Fluorescent Beads Are in Direct Contact with the Cecal Tissue *In Vivo*

(A and B) *S.*Tm^{GFP} was injected into the cecal lumen of *villin-RFP* mice. Time-lapse two-photon microscopy assessed luminal bacteria movement.

(A) Sample image. Open arrows indicate luminal *S.*Tm^{GFP}, white arrows indicate *S.*Tm^{GFP} at the tissue surface, white dashed line indicates epithelial surface.

(B) Bacterial tracks in image (A) recorded for 30 s. Red area represents cecal tissue. See also Figure S5 and Videos S8 and S9.

(C and D) *In vivo* distribution of fluorescent beads 4 h after oral gavage; imaging as in (A) and (B). Shown are representative side views (C) from the cecum and colon tissue.

(D) Quantification of the distance between fluorescent beads and epithelial surface. Each data point represents the mean of 50 beads from one image stack. Statistics: non-parametric, unpaired t test comparing the cecal and colon images. **p < 0.01. Bars indicate the mean ± SD.

establish that motile *S.*Tm penetrate the inner colon mucus layer at some sites. Although we could not directly assess the physical and biochemical properties of the mucus *in situ*, our data suggest that penetration may occur at sites featuring some type of colonic mucus layer heterogeneity. In the cecum, the mucus has gaps, exposing the epithelial surface between the crypts, which explains why this gut segment is the primary target of *S.*Tm infection in the streptomycin mouse model.

The explant imaging approach provides insights into the protective function of the mucus layer under near-native conditions. However, it should be noted that the experimental oxygen levels are higher than in the unperturbed gut, the pathogen cells have been raised *ex vivo*, and the microbiota is missing. Thus, additional information is needed to establish the relevance of our observations in the gut of mice and of other hosts of interest. Our *in vivo* control experiments could verify several key observations derived from our gut tissue explant experiments, i.e., large gaps in the cecum mucus, the preferential infection of the cecal crypt openings, and the near-surface swimming of *S.*Tm in the cecum and on top of the colonic inner mucus layer.

In line with earlier studies (Jakobsson et al., 2015; Gustafsson et al., 2012a), non-motile particles and non-flagellated *S.*Tm did not penetrate the dense inner colonic mucus layer. This probably applies to many members of the commensal microbiota, because motility genes are underrepresented in the normal human gut microbiome (Kurokawa et al., 2007), whereas flagella are associated with disease (Rooks et al., 2014; Nagao-Kitamoto et al., 2016; Okumura et al., 2016; Cullender et al., 2013). Accordingly, many enteropathogenic bacteria (e.g., *L. monocytogenes*, *V. cholerae*, *E. coli*, *S.*Tm) use flagella as a virulence factor to traverse the mucus barrier and cause infection. Flagella-driven motility can propel the pathogen toward the epithelium and accelerate disease kinetics (Stecher et al., 2004, 2008). However, several enteropathogenic bacteria lack flagella, and even some clinical *Salmonella enterica* isolates have lost their ability to express flagella (Petty et al., 2011; Andrade et al., 2002; Yang et al., 2005; Yim et al., 2011, 2014). It remains to be established if this is attributable to the costly nature of flagella expression (Soutourina and Bertin, 2003) and/or the strong immune responses elicited by flagellin (Zhao et al., 2011; Kofoed and Vance, 2011; Franchi et al., 2006; Miao et al., 2006, 2010; Koch and Barton, 2013). Non-motile pathogens could profit from peristalsis and non-continuous mucus, finding transient breaches or target regions such as Peyer's patches to access the host epithelium.

We have previously investigated how NSS affects target site selection by *S.*Tm on tissue culture cells (Misselwitz et al., 2012; Vonaesch et al., 2013). NSS plays a crucial role in this process, allowing *S.*Tm to search for cell borders and membrane ruffles, which are frequent sites for host cell invasion *in vitro*. Similarly, *S.*Tm engaged in NSS on the colonic mucus surface, which might help *S.*Tm to find sites for mucus traversal. The bacterial swimming speed was reduced within the proximal colonic inner mucus layer, suggesting that the bacteria experience drag forces when passing through the mucus. On the cecal epithelium, we observed swimming speeds that correspond to the value measured in the colon lumen, emphasizing the accessibility of the tissue at this site.

The penetration of the inner proximal colon mucus layer suggests that some sites are permissive for the traversal of motile bacterial cells. Permissiveness could be conveyed through

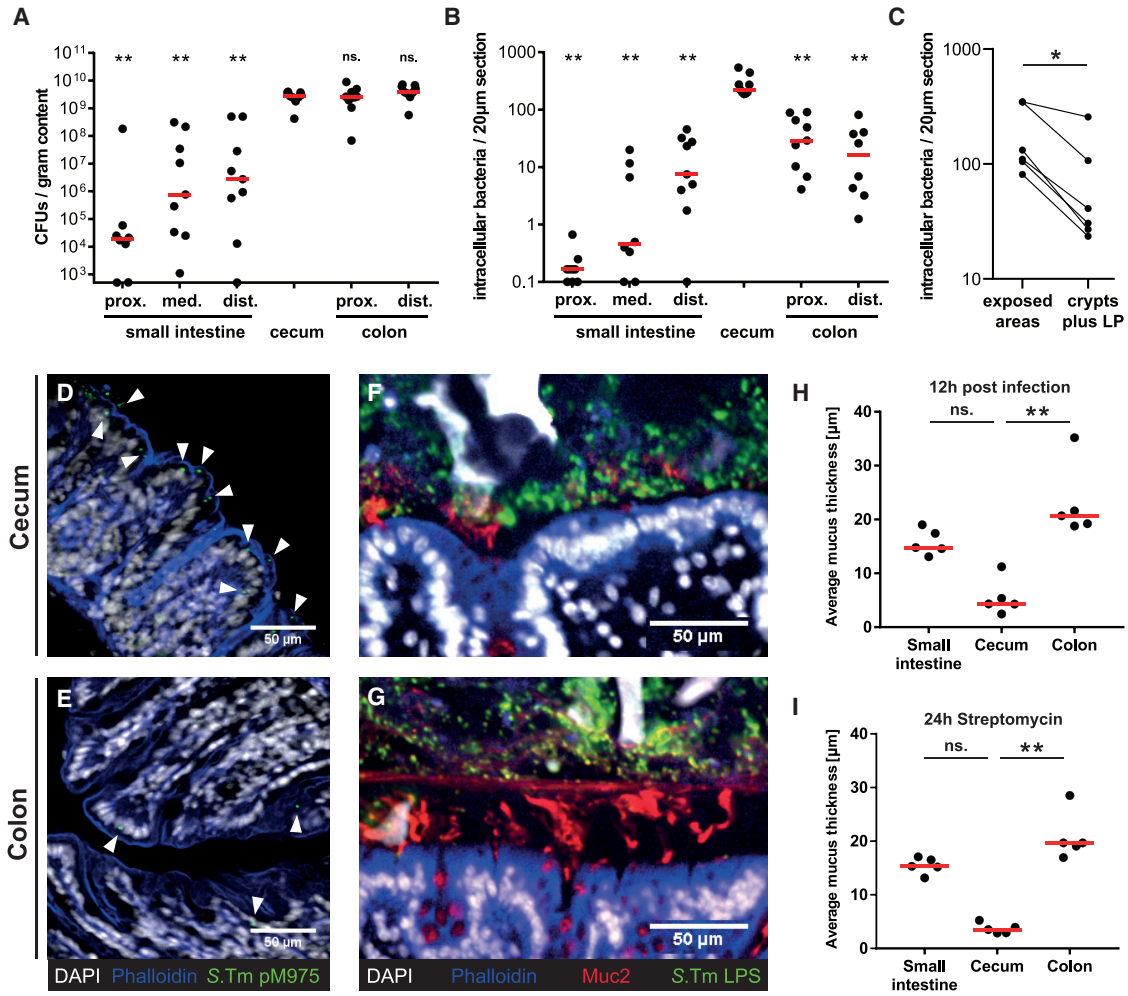

Figure 7. The Exposed Parts of the Cecum Epithelium Are the Main Site of Mucosal Invasion *In Vivo*

(A–E) Streptomycin pretreated C57BL/6 mice were infected with *S.*Tm pM975 for 12 h.

(A) *S.*Tm in the gut lumen assessed by plating. Bars indicate the median of three independent experiments.

(B) Fluorescent *S.*Tm pM975 loads in the gut tissue. Statistics: non-parametric one-way ANOVA comparing the cecum with the other gut segments. $^{**}p < 0.01$.

(C) Fluorescent *S.*Tm loads in exposed and mucus-covered parts of the cecum tissue, including the lamina propria (LP). Statistics: non-parametric, paired t test comparing the two groups. $^{*}p < 0.05$.

(D and E) Representative microscopy images of cecum (D) or colon (E) tissue. White represents DAPI; blue represents phalloidin; green represents *S.*Tm pM975, also indicated by arrowheads.

(F and G) Methacarn-fixed tissue sections from infected C57BL/6 mice. Sections were stained with antibodies against Muc2 (red) and *S.*Tm LPS (green); white represents DAPI; blue represents phalloidin. Shown are representative images from the cecum (F) and the colon (G).

(H) Thickness of the mucus layer 12 h after *S.*Tm infection (n = 5 mice). Red line indicates median.

(I) Quantification of the mucus layer thickness of non-infected C57BL/6 mice 24 h after streptomycin pretreatment. Statistics: non-parametric one-way ANOVA. $^{**}p < 0.01$.

(A and B) Bars indicate the median of three independent experiments. (H and I) Bars indicate the median. ns., not significant.

mucus heterogeneities. These may arise from the dual origin of the inner mucus layer. The renewal of the inner mucus layer is ensured by the continuous and fast secretion of mucus by the surface goblet cells (Johansson, 2012). Sentinel goblet cells, located at the crypt tips, secrete bursts of mucus by compound exocytosis upon stimulation with lipopolysaccharide, lipid A, and flagellin (Birchenough et al., 2016). The mucus from these different origins mixes in the space between the epithelium and the laminated part of the existing inner mucus layer, something that might cause irregularities in the mucus arrangement (Johansson, 2012). Such heterogeneities are then possibly exploited by motile pathogens but are harder to access by non-motile bacteria, thus further emphasizing the importance of motility for the virulence of some enteropathogenic bacteria like *S.*Tm.

A fraction of the motile *S.*Tm cells was trapped at the outer surface of the inner colonic mucus layer. This entrapment depended on bacterial motility. The inner mucus is built of Muc2 mucin nets,

staggered onto each other to generate a filter-like structure (Johansson and Hansson, 2016). This inner layer is not penetrable to bacterial-sized beads down to 0.5 μm, but well to smaller particles and molecules. *S.*Tm has a larger diameter of 0.7–1.5 μm. Entrapment of the bacterium could thus be mediated by the pore size of the mucus meshwork, trapping bacteria similar to a fishing net.

The mucus in the distal colon is turned over within 1–2 h, which is considerably faster than the stool passage (Johansson, 2012). An earlier study revealed that an accelerated mucus turnover helps to clear microbes from the gut (McLoughlin et al., 2016). Thus, trapping of pathogens followed by rapid mucus production provides an effective way to prevent bacterial infection. It will be an interesting topic for future research to determine how trapping affects the *S.*Tm infection dynamics.

In contrast with the distal murine colon, the cecum is devoid of a continuous mucus layer. This was surprising, given the importance of the colonic mucus layer in blocking microbiota access to the tissue and maintaining homeostasis. In mice, the cecal microbiota is just as dense as the one in the colon (approximately 10^{11} CFU/g), and this mass of microbes should be in direct contact with the epithelium located between the crypts. Only the bottom part of the cecal crypts is filled with mucus. This might help to protect the epithelial stem cells located at the bottom of the crypts. Indeed, most *S.*Tm invasion events occurred between cecal crypts. It remains unclear how chronic inflammation is avoided at these sites, and we can only speculate how homeostasis is maintained during encounters with the resident microbiota. The exposed epithelium might be desensitized, e.g., by downregulating innate immune receptors (Fulde et al., 2018) or by dampening of their signaling pathways (Chassin et al., 2010; Lotz et al., 2006). Cecal mucus release is controlled in part by IFN-γ signaling during the inflammatory defense and enhanced 2 days after *S.*Tm infection (Songhet et al., 2011; Zarepour et al., 2013; Jarry et al., 1994). Further studies identified the microbiota composition as a key determinant of the mucus properties (Jakobsson et al., 2015), stressing that the dynamics of mucus production and turnover are key factors in the maintenance of a healthy gut mucosa.

In summary, mucus is a highly adaptable protective barrier, with an appearance that varies considerably along the intestinal tract. Previous studies have pointed out that mucus thickness and organization vary between species (Johansson et al., 2008; Atuma et al., 2001; Szentkuti and Lorenz, 1995). Therefore, future work will have to investigate the human mucus layer in more detail to relate the present findings to human disease. Of note, the differences in cecal physiology, function (Nguyen et al., 2015), and mucus organization may help to explain why *S.*Tm does not target the same mucosal sites in different species, i.e., the human small intestine versus the cecum of the mouse. In summary, mucus architecture and mucus heterogeneities have direct consequences on the interaction between pathogens, the gut microbiota, and the host.

STAR★METHODS

Detailed methods are provided in the online version of this paper and include the following:

SUPPLEMENTAL INFORMATION

Supplemental Information can be found online at https://doi.org/10.1016/j.celrep.2019.04.106.

ACKNOWLEDGMENTS

We are grateful to the members of the Hardt lab and to Roman Stocker for helpful scientific discussions. The RCHCI staff (especially Katharina Holzinger, Dennis Mollenhauer, Alessandra Pfammatter and Sven Nowok) is gratefully acknowledged for excellent support of our animal work. Furthermore, we would like to acknowledge the support by the Scientific Center for Optical and Electron Microscopy (ScopeM) at ETH Zürich. W.-D.H. is supported by the SNF (310030_153074 and 310030B_173338/1; Sinergia CRSII_154414/1) and the Promedica Foundation, Chur. G.C.H. is supported by the European Research Council (694181), the National Institute of Allergy and Infectious Diseases (U01AI095473), The Knut and Alice Wallenberg Foundation, and the Swedish Research Council. M.E.S. received support from the Swedish Research Council (2012-262 and 2015-00635).

AUTHOR CONTRIBUTIONS

Conceptualization, M.F., M.E.S., G.C.H., and W.-D.H.; Formal Analysis, M.F.; Investigation, M.F. and M.E.S.; Resources, G.C.H.; Writing – Original Draft, M.F. and W.-D.H.; Writing – Review & Editing, M.F., M.E.S., G.C.H., and W.-D.H.; Visualization, M.F.; Funding Acquisition, W.-D.H.

DECLARATION OF INTERESTS

The authors declare no competing interests.

Received: September 5, 2018
Revised: April 1, 2019
Accepted: April 24, 2019
Published: May 28, 2019

REFERENCES

Ackermann, M., Stecher, B., Freed, N.E., Songhet, P., Hardt, W.D., and Doebeli, M. (2008). Self-destructive cooperation mediated by phenotypic noise. Nature *454*, 987–990.

Andrade, A., Girón, J.A., Amhaz, J.M., Trabulsi, L.R., and Martinez, M.B. (2002). Expression and characterization of flagella in nonmotile enteroinvasive Escherichia coli isolated from diarrhea cases. Infect. Immun. *70*, 5882–5886.

Antoni, L., Nuding, S., Weller, D., Gersemann, M., Ott, G., Wehkamp, J., and Stange, E.F. (2013). Human colonic mucus is a reservoir for antimicrobial peptides. J. Crohn's Colitis *7*, e652–e664.

Atuma, C., Strugala, V., Allen, A., and Holm, L. (2001). The adherent gastrointestinal mucus gel layer: thickness and physical state in vivo. Am. J. Physiol. Gastrointest. Liver Physiol. *280*, G922–G929.

Barr, J.J., Auro, R., Furlan, M., Whiteson, K.L., Erb, M.L., Pogliano, J., Stotland, A., Wolkowicz, R., Cutting, A.S., Doran, K.S., et al. (2013). Bacteriophage adhering to mucus provide a non-host-derived immunity. Proc. Natl. Acad. Sci. USA *110*, 10771–10776.

Barthel, M., Hapfelmeier, S., Quintanilla-Martínez, L., Kremer, M., Rohde, M., Hogardt, M., Pfeffer, K., Rüssmann, H., and Hardt, W.D. (2003). Pretreatment of mice with streptomycin provides a Salmonella enterica serovar Typhimurium colitis model that allows analysis of both pathogen and host. Infect. Immun. *71*, 2839–2858.

Bergstrom, K.S., Kissoon-Singh, V., Gibson, D.L., Ma, C., Montero, M., Sham, H.P., Ryz, N., Huang, T., Velcich, A., Finlay, B.B., et al. (2010). Muc2 protects against lethal infectious colitis by disassociating pathogenic and commensal bacteria from the colonic mucosa. PLoS Pathog. *6*, e1000902.

Bergström, J.H., Birchenough, G.M., Katona, G., Schroeder, B.O., Schütte, A., Ermund, A., Johansson, M.E., and Hansson, G.C. (2016). Gram-positive bacteria are held at a distance in the colon mucus by the lectin-like protein ZG16. Proc. Natl. Acad. Sci. USA *113*, 13833–13838.

Birchenough, G.M., Nyström, E.E., Johansson, M.E., and Hansson, G.C. (2016). A sentinel goblet cell guards the colonic crypt by triggering Nlrp6-dependent Muc2 secretion. Science *352*, 1535–1542.

Carter, P.B., and Collins, F.M. (1974). The route of enteric infection in normal mice. J. Exp. Med. *139*, 1189–1203.

Celli, J.P., Turner, B.S., Afdhal, N.H., Keates, S., Ghiran, I., Kelly, C.P., Ewoldt, R.H., McKinley, G.H., So, P., Erramilli, S., and Bansil, R. (2009). Helicobacter pylori moves through mucus by reducing mucin viscoelasticity. Proc. Natl. Acad. Sci. USA *106*, 14321–14326.

Chassin, C., Kocur, M., Pott, J., Duerr, C.U., Gütle, D., Lotz, M., and Hornef, M.W. (2010). miR-146a mediates protective innate immune tolerance in the neonate intestine. Cell Host Microbe *8*, 358–368.

Chromek, M., Arvidsson, I., and Karpman, D. (2012). The antimicrobial peptide cathelicidin protects mice from Escherichia coli O157:H7-mediated disease. PLoS ONE *7*, e46476.

Constantino, M.A., Jabbarzadeh, M., Fu, H.C., and Bansil, R. (2016). Helical and rod-shaped bacteria swim in helical trajectories with little additional propulsion from helical shape. Sci. Adv. *2*, e1601661.

Cullender, T.C., Chassaing, B., Janzon, A., Kumar, K., Muller, C.E., Werner, J.J., Angenent, L.T., Bell, M.E., Hay, A.G., Peterson, D.A., et al. (2013). Innate and adaptive immunity interact to quench microbiome flagellar motility in the gut. Cell Host Microbe *14*, 571–581.

Cummings, L.A., Wilkerson, W.D., Bergsbaken, T., and Cookson, B.T. (2006). In vivo, fliC expression by Salmonella enterica serovar Typhimurium is heterogeneous, regulated by ClpX, and anatomically restricted. Mol. Microbiol. *61*, 795–809.

Ermund, A., Gustafsson, J.K., Hansson, G.C., and Keita, A.V. (2013a). Mucus properties and goblet cell quantification in mouse, rat and human ileal Peyer's patches. PLoS ONE *8*, e83688.

Ermund, A., Schütte, A., Johansson, M.E., Gustafsson, J.K., and Hansson, G.C. (2013b). Studies of mucus in mouse stomach, small intestine, and colon. I. Gastrointestinal mucus layers have different properties depending on location as well as over the Peyer's patches. Am. J. Physiol. Gastrointest. Liver Physiol. *305*, G341–G347.

Franchi, L., Amer, A., Body-Malapel, M., Kanneganti, T.D., Ozören, N., Jagirdar, R., Inohara, N., Vandenabeele, P., Bertin, J., Coyle, A., et al. (2006). Cytosolic flagellin requires Ipaf for activation of caspase-1 and interleukin 1beta in salmonella-infected macrophages. Nat. Immunol. *7*, 576–582.

Freed, N.E., Silander, O.K., Stecher, B., Böhm, A., Hardt, W.D., and Ackermann, M. (2008). A simple screen to identify promoters conferring high levels of phenotypic noise. PLoS Genet. *4*, e1000307.

Fulde, M., Sommer, F., Chassaing, B., van Vorst, K., Dupont, A., Hensel, M., Basic, M., Klopfleisch, R., Rosenstiel, P., Bleich, A., et al. (2018). Neonatal selection by Toll-like receptor 5 influences long-term gut microbiota composition. Nature *560*, 489–493.

Gustafsson, J.K., Ermund, A., Johansson, M.E., Schütte, A., Hansson, G.C., and Sjövall, H. (2012a). An ex vivo method for studying mucus formation, properties, and thickness in human colonic biopsies and mouse small and large intestinal explants. Am. J. Physiol. Gastrointest. Liver Physiol. *302*, G430–G438.

Gustafsson, J.K., Sjövall, H., and Hansson, G.C. (2012b). Ex vivo measurements of mucus secretion by colon explants. Methods Mol. Biol. *842*, 237–243.

Haiko, J., and Westerlund-Wikström, B. (2013). The role of the bacterial flagellum in adhesion and virulence. Biology (Basel) *2*, 1242–1267.

Hapfelmeier, S., Stecher, B., Barthel, M., Kremer, M., Müller, A.J., Heikenwalder, M., Stallmach, T., Hensel, M., Pfeffer, K., Akira, S., and Hardt, W.D. (2005). The Salmonella pathogenicity island (SPI)-2 and SPI-1 type III secretion systems allow Salmonella serovar typhimurium to trigger colitis via MyD88-dependent and MyD88-independent mechanisms. J. Immunol. *174*, 1675–1685.

Hohmann, A.W., Schmidt, G., and Rowley, D. (1978). Intestinal colonization and virulence of Salmonella in mice. Infect. Immun. *22*, 763–770.

Hoiseth, S.K., and Stocker, B.A.D. (1981). Aromatic-dependent Salmonella typhimurium are non-virulent and effective as live vaccines. Nature *291*, 238–239.

Ishihara, A., Yamaguchi, S., and Hotani, H. (1981). Passive rotation of flagella on paralyzed Salmonella typhimurium (mot) mutants by external rotatory driving force. J. Bacteriol. *145*, 1082–1084.

Jakobsson, H.E., Rodríguez-Piñeiro, A.M., Schütte, A., Ermund, A., Boysen, P., Bemark, M., Sommer, F., Bäckhed, F., Hansson, G.C., and Johansson, M.E. (2015). The composition of the gut microbiota shapes the colon mucus barrier. EMBO Rep. *16*, 164–177.

Jarry, A., Merlin, D., Velcich, A., Hopfer, U., Augenlicht, L.H., and Laboisse, C.L. (1994). Interferon-gamma modulates cAMP-induced mucin exocytosis without affecting mucin gene expression in a human colonic goblet cell line. Eur. J. Pharmacol. *267*, 95–103.

Johansson, M.E. (2012). Fast renewal of the distal colonic mucus layers by the surface goblet cells as measured by in vivo labeling of mucin glycoproteins. PLoS ONE *7*, e41009.

Johansson, M.E., and Hansson, G.C. (2012). Preservation of mucus in histological sections, immunostaining of mucins in fixed tissue, and localization of bacteria with FISH. Methods Mol. Biol. *842*, 229–235.

Johansson, M.E., and Hansson, G.C. (2016). Immunological aspects of intestinal mucus and mucins. Nat. Rev. Immunol. *16*, 639–649.

Johansson, M.E., Phillipson, M., Petersson, J., Velcich, A., Holm, L., and Hansson, G.C. (2008). The inner of the two Muc2 mucin-dependent mucus layers in colon is devoid of bacteria. Proc. Natl. Acad. Sci. USA *105*, 15064–15069.

Johansson, M.E., Gustafsson, J.K., Sjöberg, K.E., Petersson, J., Holm, L., Sjövall, H., and Hansson, G.C. (2010). Bacteria penetrate the inner mucus layer before inflammation in the dextran sulfate colitis model. PLoS ONE *5*, e12238.

Johansson, M.E., Larsson, J.M., and Hansson, G.C. (2011). The two mucus layers of colon are organized by the MUC2 mucin, whereas the outer layer is a legislator of host-microbial interactions. Proc. Natl. Acad. Sci. USA *108* (*Suppl 1*), 4659–4665.

Johansson, M.E., Gustafsson, J.K., Holmén-Larsson, J., Jabbar, K.S., Xia, L., Xu, H., Ghishan, F.K., Carvalho, F.A., Gewirtz, A.T., Sjövall, H., and Hansson, G.C. (2014). Bacteria penetrate the normally impenetrable inner colon mucus layer in both murine colitis models and patients with ulcerative colitis. Gut *63*, 281–291.

Kaiser, P., Diard, M., Stecher, B., and Hardt, W.D. (2012). The streptomycin mouse model for Salmonella diarrhea: functional analysis of the microbiota, the pathogen's virulence factors, and the host's mucosal immune response. Immunol. Rev. *245*, 56–83.

Kamphuis, J.B.J., Mercier-Bonin, M., Eutamène, H., and Theodorou, V. (2017). Mucus organisation is shaped by colonic content; a new view. Sci. Rep. *7*, 8527.

Koch, M.A., and Barton, G.M. (2013). TLR5 stops commensals in their tracks. Cell Host Microbe *14*, 488–490.

Kofoed, E.M., and Vance, R.E. (2011). Innate immune recognition of bacterial ligands by NAIPs determines inflammasome specificity. Nature *477*, 592–595.

Koirala, S., Mears, P., Sim, M., Golding, I., Chemla, Y.R., Aldridge, P.D., and Rao, C.V. (2014). A nutrient-tunable bistable switch controls motility in Salmonella enterica serovar Typhimurium. MBio *5*, e01611–e01614.

Kurokawa, K., Itoh, T., Kuwahara, T., Oshima, K., Toh, H., Toyoda, A., Takami, H., Morita, H., Sharma, V.K., Srivastava, T.P., et al. (2007). Comparative metagenomics revealed commonly enriched gene sets in human gut microbiomes. DNA Res. *14*, 169–181.

Lara-Tejero, M., and Galán, J.E. (2009). Salmonella enterica serovar typhimurium pathogenicity island 1-encoded type III secretion system translocases mediate intimate attachment to nonphagocytic cells. Infect. Immun. *77*, 2635–2642.

Lauga, E., DiLuzio, W.R., Whitesides, G.M., and Stone, H.A. (2006). Swimming in circles: motion of bacteria near solid boundaries. Biophys. J. *90*, 400–412.

Li, H., Limenitakis, J.P., Fuhrer, T., Geuking, M.B., Lawson, M.A., Wyss, M., Brugiroux, S., Keller, I., Macpherson, J.A., Rupp, S., et al. (2015). The outer mucus layer hosts a distinct intestinal microbial niche. Nat. Commun. *6*, 8292.

Li, X., Bleumink-Pluym, N.M.C., Luijkx, Y.M.C.A., Wubbolts, R.W., van Putten, J.P.M., and Strijbis, K. (2019). MUC1 is a receptor for the Salmonella SiiE adhesin that enables apical invasion into enterocytes. PLoS Pathog. *15*, e1007566.

Lotz, M., Gütle, D., Walther, S., Ménard, S., Bogdan, C., and Hornef, M.W. (2006). Postnatal acquisition of endotoxin tolerance in intestinal epithelial cells. J. Exp. Med. *203*, 973–984.

Luche, H., Weber, O., Nageswara Rao, T., Blum, C., and Fehling, H.J. (2007). Faithful activation of an extra-bright red fluorescent protein in "knock-in" Cre-reporter mice ideally suited for lineage tracing studies. Eur. J. Immunol. *37*, 43–53.

Madison, B.B., Dunbar, L., Qiao, X.T., Braunstein, K., Braunstein, E., and Gumucio, D.L. (2002). Cis elements of the villin gene control expression in restricted domains of the vertical (crypt) and horizontal (duodenum, cecum) axes of the intestine. J. Biol. Chem. *277*, 33275–33283.

McLoughlin, K., Schluter, J., Rakoff-Nahoum, S., Smith, A.L., and Foster, K.R. (2016). Host Selection of Microbiota via Differential Adhesion. Cell Host Microbe *19*, 550–559.

Meyer-Hoffert, U., Hornef, M.W., Henriques-Normark, B., Axelsson, L.G., Midtvedt, T., Pütsep, K., and Andersson, M. (2008). Secreted enteric antimicrobial activity localises to the mucus surface layer. Gut *57*, 764–771.

Miao, E.A., Alpuche-Aranda, C.M., Dors, M., Clark, A.E., Bader, M.W., Miller, S.I., and Aderem, A. (2006). Cytoplasmic flagellin activates caspase-1 and secretion of interleukin 1beta via Ipaf. Nat. Immunol. *7*, 569–575.

Miao, E.A., Mao, D.P., Yudkovsky, N., Bonneau, R., Lorang, C.G., Warren, S.E., Leaf, I.A., and Aderem, A. (2010). Innate immune detection of the type III secretion apparatus through the NLRC4 inflammasome. Proc. Natl. Acad. Sci. USA *107*, 3076–3080.

Michalet, X. (2010). Mean square displacement analysis of single-particle trajectories with localization error: Brownian motion in an isotropic medium. Phys. Rev. E Stat. Nonlin. Soft Matter Phys. *82*, 041914.

Misselwitz, B., Dilling, S., Vonaesch, P., Sacher, R., Snijder, B., Schlumberger, M., Rout, S., Stark, M., von Mering, C., Pelkmans, L., and Hardt, W.D. (2011a). RNAi screen of Salmonella invasion shows role of COPI in membrane targeting of cholesterol and Cdc42. Mol. Syst. Biol. *7*, 474.

Misselwitz, B., Kreibich, S.K., Rout, S., Stecher, B., Periaswamy, B., and Hardt, W.D. (2011b). Salmonella enterica serovar Typhimurium binds to HeLa cells via Fim-mediated reversible adhesion and irreversible type three secretion system 1-mediated docking. Infect. Immun. *79*, 330–341.

Misselwitz, B., Barrett, N., Kreibich, S., Vonaesch, P., Andritschke, D., Rout, S., Weidner, K., Sormaz, M., Songhet, P., Horvath, P., et al. (2012). Near surface swimming of Salmonella Typhimurium explains target-site selection and cooperative invasion. PLoS Pathog. *8*, e1002810.

Müller, A.J., Kaiser, P., Dittmar, K.E., Weber, T.C., Haueter, S., Endt, K., Songhet, P., Zellweger, C., Kremer, M., Fehling, H.J., and Hardt, W.D. (2012). Salmonella gut invasion involves TTSS-2-dependent epithelial traversal, basolateral exit, and uptake by epithelium-sampling lamina propria phagocytes. Cell Host Microbe *11*, 19–32.

Muniz, L.R., Knosp, C., and Yeretssian, G. (2012). Intestinal antimicrobial peptides during homeostasis, infection, and disease. Front. Immunol. *3*, 310.

Nagao-Kitamoto, H., Shreiner, A.B., Gillilland, M.G., 3rd, Kitamoto, S., Ishii, C., Hirayama, A., Kuffa, P., El-Zaatari, M., Grasberger, H., Seekatz, A.M., et al. (2016). Functional Characterization of Inflammatory Bowel Disease-Associated Gut Dysbiosis in Gnotobiotic Mice. Cell. Mol. Gastroenterol. Hepatol. *2*, 468–481.

Nguyen, T.L.A., Vieira-Silva, S., Liston, A., and Raes, J. (2015). How informative is the mouse for human gut microbiota research? Dis. Model. Mech. *8*, 1–16.

Okumura, R., Kurakawa, T., Nakano, T., Kayama, H., Kinoshita, M., Motooka, D., Gotoh, K., Kimura, T., Kamiyama, N., Kusu, T., et al. (2016). Lypd8 promotes the segregation of flagellated microbiota and colonic epithelia. Nature *532*, 117–121.

Petersson, J., Schreiber, O., Hansson, G.C., Gendler, S.J., Velcich, A., Lundberg, J.O., Roos, S., Holm, L., and Phillipson, M. (2011). Importance and regulation of the colonic mucus barrier in a mouse model of colitis. Am. J. Physiol. Gastrointest. Liver Physiol. *300*, G327–G333.

Petty, N.K., Feltwell, T., Pickard, D., Clare, S., Toribio, A.L., Fookes, M., Roberts, K., Monson, R., Nair, S., Kingsley, R.A., et al. (2011). Citrobacter rodentium is an unstable pathogen showing evidence of significant genomic flux. PLoS Pathog. *7*, e1002018.

Porwollik, S., Santiviago, C.A., Cheng, P., Long, F., Desai, P., Fredlund, J., Srikumar, S., Silva, C.A., Chu, W., Chen, X., et al. (2014). Defined single-gene and multi-gene deletion mutant collections in Salmonella enterica sv Typhimurium. PLoS ONE *9*, e99820.

Qi, M., Gong, X., Wu, B., and Zhang, G. (2017). Landing Dynamics of Swimming Bacteria on a Polymeric Surface: Effect of Surface Properties. Langmuir *33*, 3525–3533.

Rooks, M.G., Veiga, P., Wardwell-Scott, L.H., Tickle, T., Segata, N., Michaud, M., Gallini, C.A., Beal, C., van Hylckama-Vlieg, J.E., Ballal, S.A., et al. (2014). Gut microbiome composition and function in experimental colitis during active disease and treatment-induced remission. ISME J. *8*, 1403–1417.

Schultsz, C., Van Den Berg, F.M., Ten Kate, F.W., Tytgat, G.N., and Dankert, J. (1999). The intestinal mucus layer from patients with inflammatory bowel disease harbors high numbers of bacteria compared with controls. Gastroenterology *117*, 1089–1097.

Sellin, M.E., Müller, A.A., Felmy, B., Dolowschiak, T., Diard, M., Tardivel, A., Maslowski, K.M., and Hardt, W.D. (2014). Epithelium-intrinsic NAIP/NLRC4 inflammasome drives infected enterocyte expulsion to restrict Salmonella replication in the intestinal mucosa. Cell Host Microbe *16*, 237–248.

Songhet, P., Barthel, M., Stecher, B., Müller, A.J., Kremer, M., Hansson, G.C., and Hardt, W.D. (2011). Stromal IFN-γR-signaling modulates goblet cell function during Salmonella Typhimurium infection. PLoS ONE *6*, e22459.

Soutourina, O.A., and Bertin, P.N. (2003). Regulation cascade of flagellar expression in Gram-negative bacteria. FEMS Microbiol. Rev. *27*, 505–523.

Stecher, B., Hapfelmeier, S., Müller, C., Kremer, M., Stallmach, T., and Hardt, W.D. (2004). Flagella and chemotaxis are required for efficient induction of Salmonella enterica serovar Typhimurium colitis in streptomycin-pretreated mice. Infect. Immun. *72*, 4138–4150.

Stecher, B., Barthel, M., Schlumberger, M.C., Haberli, L., Rabsch, W., Kremer, M., and Hardt, W.D. (2008). Motility allows S. Typhimurium to benefit from the mucosal defence. Cell. Microbiol. *10*, 1166–1180.

Swidsinski, A., Weber, J., Loening-Baucke, V., Hale, L.P., and Lochs, H. (2005). Spatial organization and composition of the mucosal flora in patients with inflammatory bowel disease. J. Clin. Microbiol. *43*, 3380–3389.

Szentkuti, L., and Lorenz, K. (1995). The thickness of the mucus layer in different segments of the rat intestine. Histochem. J. *27*, 466–472.

Tinevez, J.Y., Perry, N., Schindelin, J., Hoopes, G.M., Reynolds, G.D., Laplantine, E., Bednarek, S.Y., Shorte, S.L., and Eliceiri, K.W. (2017). TrackMate: An open and extensible platform for single-particle tracking. Methods *115*, 80–90.

Valdivia, R.H., and Falkow, S. (1996). Bacterial genetics by flow cytometry: rapid isolation of Salmonella typhimurium acid-inducible promoters by differential fluorescence induction. Mol. Microbiol. *22*, 367–378.

Van der Sluis, M., De Koning, B.A., De Bruijn, A.C., Velcich, A., Meijerink, J.P., Van Goudoever, J.B., Büller, H.A., Dekker, J., Van Seuningen, I., Renes, I.B., and Einerhand, A.W. (2006). Muc2-deficient mice spontaneously develop colitis, indicating that MUC2 is critical for colonic protection. Gastroenterology *131*, 117–129.

Vonaesch, P., Cardini, S., Sellin, M.E., Goud, B., Hardt, W.D., and Schauer, K. (2013). Quantitative insights into actin rearrangements and bacterial target site selection from Salmonella Typhimurium infection of micropatterned cells. Cell. Microbiol. *15*, 1851–1865.

Wotzka, S.Y., Nguyen, B.D., and Hardt, W.D. (2017). Salmonella Typhimurium Diarrhea Reveals Basic Principles of Enteropathogen Infection and Disease-Promoted DNA Exchange. Cell Host Microbe *21*, 443–454.

Yang, F., Yang, J., Zhang, X., Chen, L., Jiang, Y., Yan, Y., Tang, X., Wang, J., Xiong, Z., Dong, J., et al. (2005). Genome dynamics and diversity of Shigella species, the etiologic agents of bacillary dysentery. Nucleic Acids Res. *33*, 6445–6458.

Yim, L., Betancor, L., Martínez, A., Bryant, C., Maskell, D., and Chabalgoity, J.A. (2011). Naturally occurring motility-defective mutants of Salmonella enterica serovar Enteritidis isolated preferentially from nonhuman rather than human sources. Appl. Environ. Microbiol. *77*, 7740–7748.

Yim, L., Sasías, S., Martínez, A., Betancor, L., Estevez, V., Scavone, P., Bielli, A., Sirok, A., and Chabalgoity, J.A. (2014). Repression of flagella is a common trait in field isolates of Salmonella enterica serovar Dublin and is associated with invasive human infections. Infect. Immun. *82*, 1465–1476.

Zarepour, M., Bhullar, K., Montero, M., Ma, C., Huang, T., Velcich, A., Xia, L., and Vallance, B.A. (2013). The mucin Muc2 limits pathogen burdens and epithelial barrier dysfunction during Salmonella enterica serovar Typhimurium colitis. Infect. Immun. *81*, 3672–3683.

Zhao, Y., Yang, J., Shi, J., Gong, Y.N., Lu, Q., Xu, H., Liu, L., and Shao, F. (2011). The NLRC4 inflammasome receptors for bacterial flagellin and type III secretion apparatus. Nature *477*, 596–600.

STAR★METHODS

KEY RESOURCES TABLE

REAGENT or RESOURCE	SOURCE	IDENTIFIER
Antibodies		
Rabbit polyclonal anti-*Salmonella* O5	Becton Dickinson	Cat#226601
Rabbit polyclonal anti-Mucin 2	Santa Cruz Biotechnology	Cat#sc-15334; RRID: AB_2146667
Goat polyclonal anti-Rabbit Fab, Cy3 conjugate	Jackson ImmunoResearch Labs	Cat# 111-167-003; RRID: AB_2313593
Goat polyclonal anti-Rabbit, Cy5 conjugate	Jackson ImmunoResearch Labs	Cat# 111-175-144; RRID:AB_2338013
Bacterial and Virus Strains		
S. Tm, strain: SL1344	Hoiseth and Stocker, 1981	Cat#SL1344; RRID: WB-STRAIN:SL1344
S. Tm$^{\Delta fliGHI}$, strain: M913	Stecher et al., 2004	N/A
S. Tm$^{\Delta motA}$, strain: Z1403	This study	N/A
Chemicals, Peptides, and Recombinant Proteins		
Wheat germ agglutinin, AF647 conjugate	Invitrogen	Cat#W32466
Fluoresbrite YG Microspheres, 2 μm	Polysciences	Cat#18338-5
Histoacryl (blue) tissue adhesive	B.Braun	Cat#1050052
Experimental Models: Organisms/Strains		
Mouse: C57BL/6J	The Jackson Laboratory	Cat#JAX:000664; RRID: IMSR_JAX:000664
Mouse: RedMUC2^{98trTG}	Birchenough et al., 2016	N/A
Mouse: B6.B6-Gt(ROSA)26Sortm1Hjf x B6.SJL-Tg(Vil-cre)997Gum/J	Madison et al., 2002; Luche et al., 2007; Müller et al., 2012	N/A
Recombinant DNA		
Plasmid: pM965	Stecher et al., 2004	N/A
Plasmid:pM975	Hapfelmeier et al., 2005	N/A
Plasmid: pFPV25.5 mCherry	This study	N/A
Software and Algorithms		
Fiji/ImageJ	open source Java image processing program	https://imagej.nih.gov/ij/
Trackmate ImageJ plugin	Tinevez et al., 2017	https://github.com/fiji/TrackMate/releases/tag/TrackMate_-3.5.3
Prism8 statistical analysis software	GraphPad	https://www.graphpad.com
Other		
Confocal microscope	Zeiss	LSM880
Water dipping objective	Zeiss	Achroplan 20x/0.5W Ph2; Cat#440049
Confocal microscope	Leica	SP8 DMI6000B
Multiphoton laser	Spectra-Physics	Mai Tai XF
Multiphoton laser	Spectra-Physics	InSight DeepSee
Confocal microscope	Zeiss	Axiovert 200 m

CONTACT FOR REAGENT AND RESOURCE SHARING

Further information and requests for resources or reagents should be directed to the Lead Contact, Wolf-Dietrich Hardt (hardt@micro.biol.ethz.ch). Primary image data is available upon reasonable request.

EXPERIMENTAL MODEL AND SUBJECT DETAILS

Animals

C57BL/6 and *villin-RFP* mice (Müller et al., 2012; Madison et al., 2002; Luche et al., 2007) were held under specific pathogen free (SPF) conditions at the EPIC facility at ETH Zürich. *RedMUC2*^{98trTg} mice (Birchenough et al., 2016) were held under SPF conditions at the RCHCI facility at ETH Zürich. All animal experiments were approved and overseen by Kantonales Veterinäramt Zürich, Zürich, Switzerland (License 193/2016) and comply with the cantonal and Swiss legislation. Both, female and male mice aged 8-12 weeks were used in the experiments due to animal welfare reasons. Mice of both sexes were randomly assigned to experimental groups.

Bacterial strains and culture conditions

SL1344 was used as WT strain (Hoiseth and Stocker, 1981). *S.*Tm$^{\Delta fliGHI}$ was described elsewhere (Stecher et al., 2004). *S.*Tm$^{\Delta motA}$ was generated by P22-transduction of a kanamycin resistant *ΔmotA* mutant (Porwollik et al., 2014) into SL1344. The green fluorescent reporter plasmids pM965 (*rpsM* promoter) and pM975 (*ssaG* promoter) were described earlier (Stecher et al., 2004; Hapfelmeier et al., 2005). The constitutively red fluorescent reporter plasmid is a derivative of pFPV25.1 (Valdivia and Falkow, 1996), where the GFP cassette was replaced with mCherry.

Bacterial cultures were grown for 12h at 37°C in LB medium containing 0.3M NaCl, subcultured for 4h at 37°C and resuspended in PBS prior to use.

METHOD DETAILS

Streptomycin mouse model

8-12 week old mice were orally pretreated with streptomycin (25 mg) 24 h prior to infection. Infection was performed by oral gavage of $5 \cdot 10^7$ cfu *S.*Tm. Mice were sacrificed by CO_2 asphyxiation or cervical dislocation 12 h post infection.

Histological Methods

For counting of the *S.*Tm tissue loads, small intestinal, cecal and colon tissue was excised, fixed in 4% paraformaldehyde (w/v in PBS) for 5 h at room temperature, followed by 24 h in 20% sucrose solution (w/v in PBS) at 4°C. The samples were embedded and frozen in Tissue-Tek OCT medium (Sysmex). 20 μm sections of these cryoblocks were cut and stained using DAPI and TRITC-Phalloidin.

For mucus staining, intestinal tissue was excised and directly fixed in freshly prepared Methacarn solution (60% methanol, 30% chloroform, 10% glacial acetic acid) for 24 to 72 h. The samples were transferred to pure methanol for 2 h and kept for 30, 60 and again 60 min in subsequent baths of 100% ethanol at 37°C. This was followed by 30, 45 and 60 min in Xylol at 37°C and 45, 60 and 60 min in paraffin at 62°C. 10 μm sections were cut from paraffin blocks and dried on polysine coated slides (Fischer Scientific) overnight. Slides were deparaffinized for 20 min in Xylene substitute solution (Sigma) and rehydrated by 5 min incubation steps in 100, 95, 70, 50 and 30% ethanol and PBS. Slides were sequentially stained using a rabbit anti *S.*Tm LPS antiserum (Difco), goat anti rabbit Cy3 Fab fragment (Jackson), anti Muc2 (Santa Cruz Biotechnology) and goat anti rabbit Cy5 (Jackson) antibodies as well as DAPI. As an alternative for the Muc2 antibodies, fluorescently labeled Wheat germ agglutinin (WGA) was used for mucus staining.

Images of fixed tissues were recorded using a confocal Zeiss Axiovert 200 m microscope with two evolve 512 EMCCD cameras (Photometrics) and a 20x air objective.

Explant microscopy setup

Explant tissues were imaged using an upright Zeiss LSM 880 laser scanning microscope. For these images, a Zeiss Achroplan 20x water dipping objective was used. Live-imaging was performed at framerates of 0.166 s (*S.*Tm) or 0.615 s respectively (*S.*Tm$^{\Delta fliGHI}$ and *S.*Tm$^{\Delta motA}$).

For live-imaging of explanted mouse tissues, mice were sacrificed by cervical dislocation and the intestine was excised. 2 cm parts of the terminal ileum, cecum or distal colon were opened lengthwise and the intestinal contents were removed by careful agitation in Krebs buffer. The tissue was attached to the bottom of a Petri dish using tissue glue (Histoacryl, Braun) with the luminal side facing up and covered with Krebs buffer. *S.*Tm^{GFP} (10^7 cfu) was added dropwise to the buffer and imaging was completed within $\leq$ 30 min of sacrificing the mouse. This ensured tissue and mucus integrity without interference from mucosal degradation.

FITC-coated (Polysciences Inc.) latex beads (2μm diameter) were diluted 1:20 and added dropwise to the liquid covering the tissue. Beads were allowed to sediment for 2 min prior to imaging.

*S.*Tm was grown as indicated above. The culture was resuspended in Krebs buffer and diluted 1:5. 50 μl of this solution were added to the liquid covering the tissue. Bacteria were allowed to distribute in the sample for 2 min. prior to imaging.

Intra-vital microscopy

Intra-vital microscopy was performed as previously described (Sellin et al., 2014; Müller et al., 2012). In short, mice were initially anaesthetized by intravenous injection of Propofol. Subsequently, the mice were intubated and held under continuous isoflurane anesthesia (1.8 - 1.9% isoflurane). The cecum or colon tissue was exposed and inserted into a custom-made microscopy stage.

*S.*Tm^{GFP} was not detectable upon oral gavage due to its low fluorescence intensity in the anaerobic intestine. Thus, we injected 50 μl *S.*Tm^{GFP} from the bottom of a 4h subculture, as described above, directly into the cecal lumen. The cecum was gently massaged to mix the injected solution with the cecal content and equilibrated for 15 minutes prior to imaging. Following equilibration, we tracked individual gut luminal *S.*Tm over time via two-photon microscopy through the intact cecal wall. Images were acquired with a Leica SP8 DMI6000B microscope equipped with a Mai Tai XF and an InSight DeepSee laser unit (spectra-Physics). Fluorescence was detected with an external two-channel NDD detector unit with two Leica HyD detectors. Mouse health and anesthesia was monitored throughout the experiment. After the experiment, the mice were sacrificed by cervical dislocation. For fluorescent bead detection, mice were gavaged with 100 μl of FITC-coated latex beads (Polysciences Inc.) of 2 μm diameter 4h prior to imaging.

QUANTIFICATION AND STATISTICAL ANALYSIS

Image Analysis

Distance measurements on Methacarn fixed slides were done manually using Fiji/ImageJ. Mucus thickness was measured at 5 points per image on at least five images per mouse.

Image stacks from explant microscopy samples were resliced in Z-direction. A maximum intensity projection of the image was used to visualize the distance of *S.*Tm or fluorescent beads (green fluorescence) to the tissue (red fluorescence).

*S.*Tm in different regions above the tissue explants were counted using a customized ImageJ macro. In short, fluorescent *S.*Tm were enumerated in consecutive image planes perpendicular to the tissue, each spaced 5 μm apart. The image stack was then divided into four different regions (Figures 2F and 2G): The tissue surface (T; 10 μm centered around the topmost image plain covered 50% with epithelium), the inner mucus layer of variable thickness (IM; region between T and Z) and the surface of the inner mucus layer (Z; slice of 15 μm above the lower edge of the zone of *S.*Tm accumulation). As a fourth region, we quantified *S.*Tm in the lumen / loose mucus (L) up to 50 μm above Z.

Bacterial motion was analyzed using the ImageJ plugin Trackmate. A blob size of 2.2 μm was set as size constraint for bacterial detection. Occasionally, tracks had to be manually corrected due to incorrect linking. Tracking data was exported and the mean square distance was calculated for each track. Bacterial motion was categorized by plotting the MSD data for each track using GraphPad Prism. The frequency of NSS, straight swimming, diffusion and trapping were quantified based on the optical appearance of the tracks, as illustrated (Figure S1B). Linear regression was performed with the MSD data for the first 10 time intervals. The diffusion coefficient was then calculated as 1/4 times the slope of the regression line (Michalet, 2010). *S.*Tm swimming speeds were directly obtained from the tracking data exported from Trackmate.

Statistical analysis

All datasets were analyzed using GraphPad Prism8. Statistical details such as the test used and the number of animals and replicates are stated in the figure legends. In general, we used a non-parametric 1-way ANOVA to compare between different groups. In Figure S3, we use a Wilcoxon signed rank test to assess whether the dataset is significantly different from 1. We show the mean ± SD in scatter dot plots and the median and quartiles for violin plots. In Figures 5F and 7, we indicate the median of all mice measured instead. p values above 0.05 were considered non significant (ns.). Lower p values were classified as * ($p < 0.05$) and ** ($p < 0.01$).

Cell Reports, Volume *27*

Supplemental Information

Mucus Architecture and Near-Surface Swimming Affect Distinct *Salmonella* Typhimurium Infection Patterns along the Murine Intestinal Tract

Markus Furter, Mikael E. Sellin, Gunnar C. Hansson, and Wolf-Dietrich Hardt

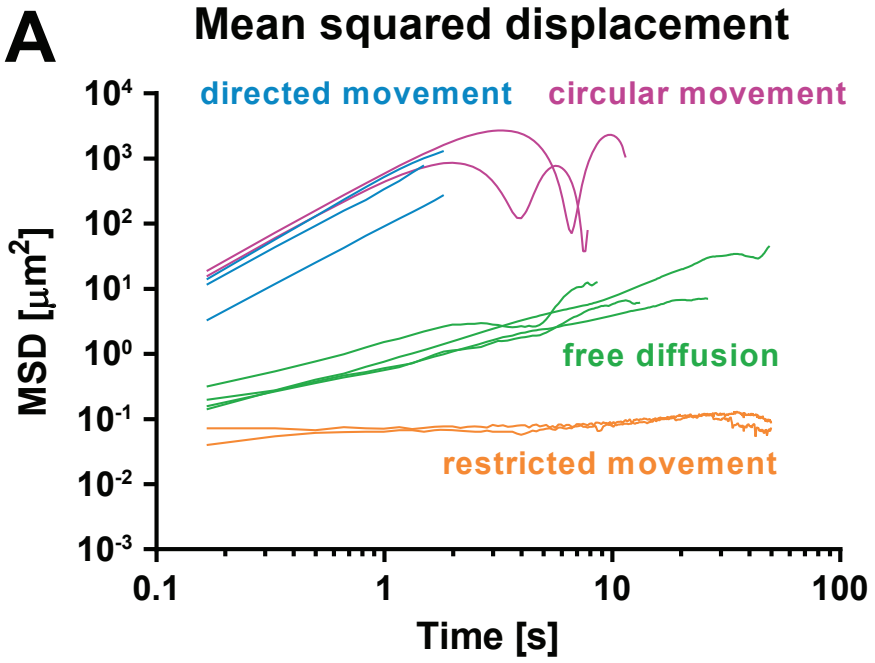
A
Mean squared displacement
directed movement
circular movement
free diffusion
restricted movement
MSD [μm²]
10⁴
10³
10²
10¹
10⁰
10⁻¹
10⁻²
10⁻³
0.1
1
10
100
Time [s]

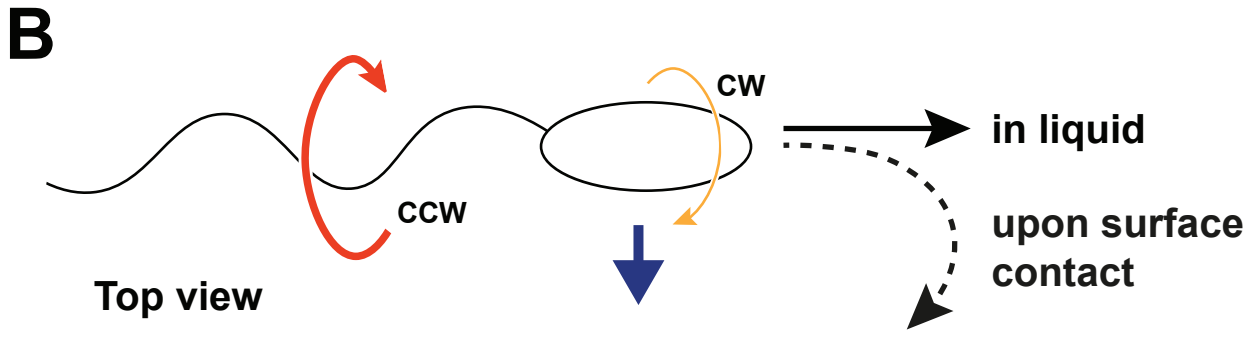
B
CW
CCW
Top view
in liquid
upon surface contact

Fig. S1, related to Fig. 1: Measuring bacterial near surface swimming with the mean squared displacement. (A) The mean squared displacement (MSD) is a way to characterize the random walk of particles in 1 to 3 dimensions. For each time interval possible, the average distance travelled (squared, to avoid negative values) is calculated and plotted on the MSD graph. Particles that are constrained in their movement or move slowly produce a slight slope whereas freely diffusing and actively moving particles have steeper slopes. The circular motion during NSS generates an oscillating curve since the bacterium repeatedly returns to the origin of its trajectory. (B) Schematic drawing of the forces exerted on bacteria during near surface swimming (NSS). The torque of the flagella rotating counter-clockwise (CCW, Red arrow) induces a slower rotation of the bacterial body in the opposite direction (CW, yellow arrow). Upon contact with a surface, the rotation of the bacterial body generates a perpendicular force (blue arrow) that diverts the bacterium from its linear to a circular track.

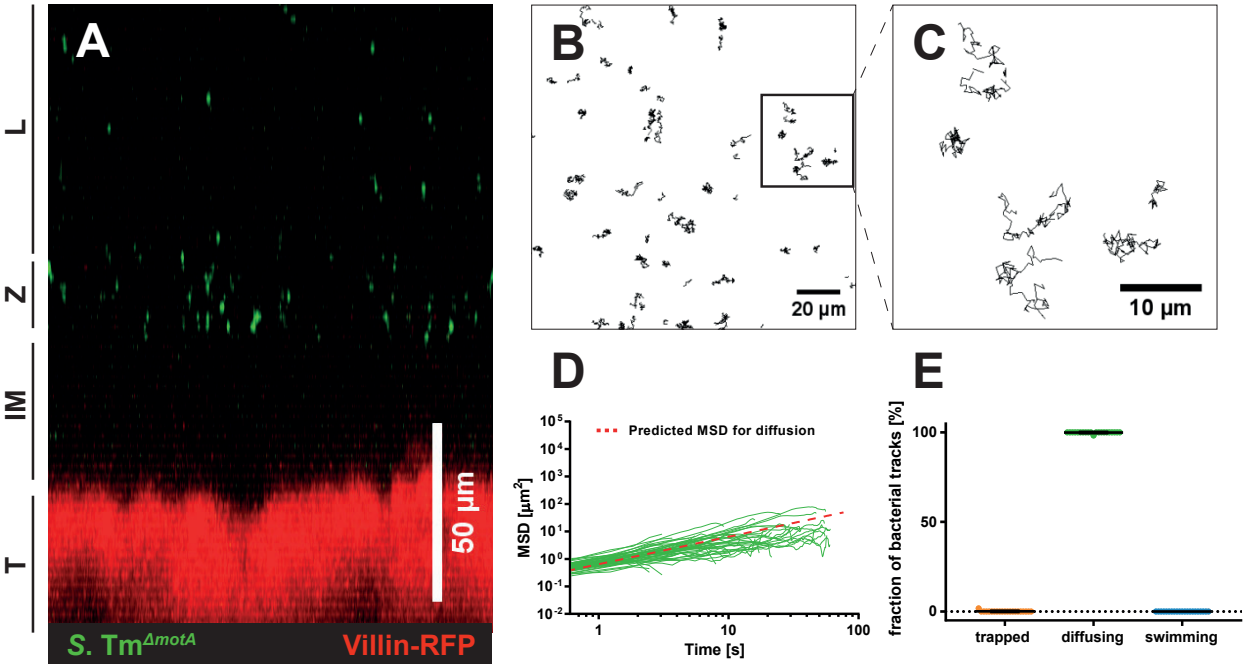
A
L
Z
IM
T
50 µm
S. Tm ΔmotA
Villin-RFP
B
20 µm
C
10 µm
D
Predicted MSD for diffusion
MSD [µm²]
Time [s]
E
fraction of bacterial tracks [%]
trapped
diffusing
swimming

Fig. S2, related to Fig. 2: *S.*Tm$^{\Delta motA}$ is not trapped in the mucus layer. Distal colon tissue samples were excised from untreated *villin-RFP* mice and mounted on a petri dish. After mounting, green fluorescent *S.*Tm were added onto the tissue and confocal image stacks were acquired. (A) Side-view of a confocal z-stack after addition of *S.*Tm$^{\Delta motA}$. The image is labeled as in Fig. 1. (B) Time-lapse imaging of the mucus surface in image stack (A). The tracks of the bacteria on the mucus are shown in black. (C) Magnification of the area marked in (B). (D) Mean Squared Displacement (MSD) calculated from 50 random *S.*Tm$^{\Delta motA}$ tracks at the colon mucus surface. The plot is color-coded for the motility phenotype of each track as in Fig. 1. (E) Trapped, diffusing and swimming *S.*Tm were quantified manually based on optical appearance of the tracks. Depicted is the mean ± SD from three independent experiments.

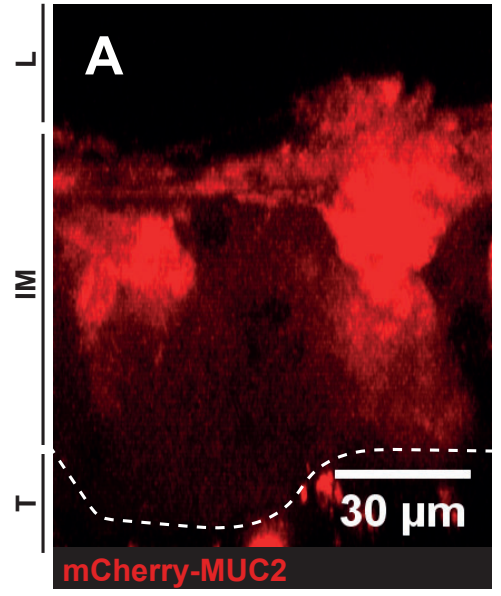
A
L
IM
T
30 µm
mCherry-MUC2

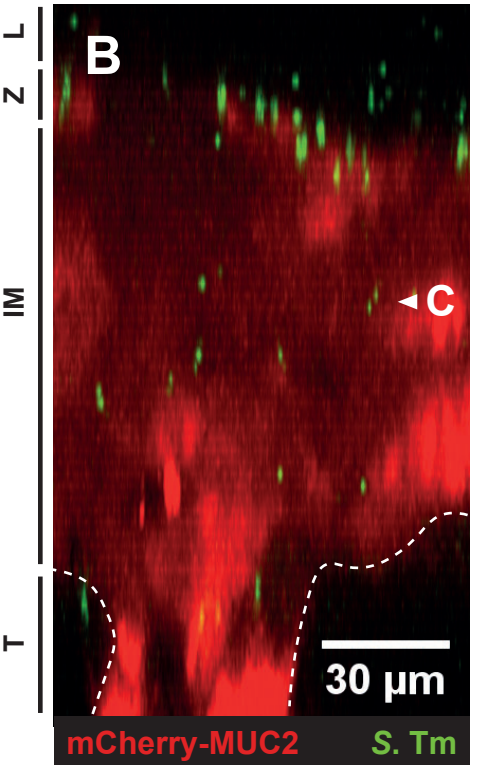
B
L
Z
IM
T
C
30 µm
mCherry-MUC2
S. Tm

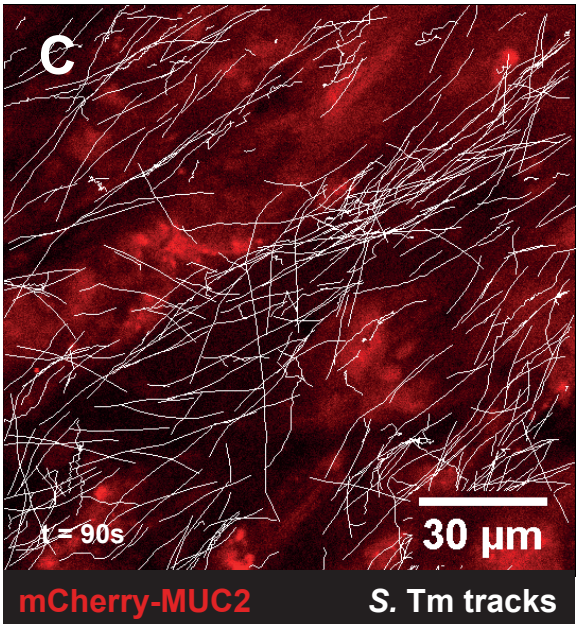
C
t = 90s
30 µm
mCherry-MUC2
S. Tm tracks

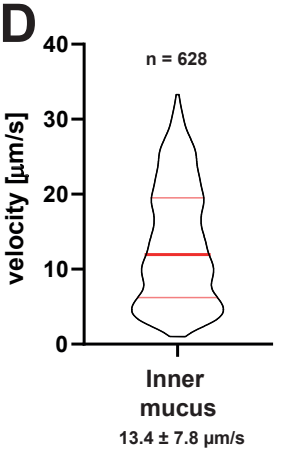
D
n = 628
velocity [µm/s]
40
30
20
10
0
Inner
mucus
13.4 ± 7.8 µm/s

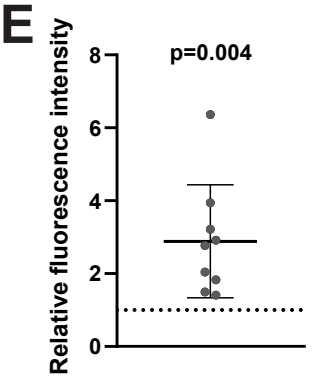
E
p=0.004
Relative fluorescence intensity
8
6
4
2
0

Fig. S3, related to Fig. 4: *S.*Tm can probe for heterogeneities to penetrate the mucus. This proof of principle-type experiment visualizes *S.*Tm interactions with inner mucus layer heterogeneities. For this purpose, we used distal colon explants of *RedMUC2*^{98trTg} mice. These mice show an uneven, aberrant mucus distribution, caused by the presence of both, the native murine Muc2 and mCherry-tagged human MUC2. It is important to note that this heterogeneous mucus does not represent the situation in wild type mice, and is a specific artefact of the *RedMUC2*^{98trTg} mice. (A) Explant imaging of distal colon samples from untreated *RedMUC2*^{98trTg} mice, revealing uneven distribution of the fluorescent signal. It is currently not clear, whether dimly fluorescent areas are enriched with unlabeled, murine mucus or have an overall lower mucus density. Shown is the side-view of a representative confocal z-stack. Labels indicate the tissue (T), inner mucus layer (IM) and the lumen / loose mucus (L). (B-E) Distal colon tissue from untreated *RedMUC2*^{98trTg} mice was infected with *S.*Tm^{GFP}. (B) Side-view of a confocal z-stack after addition of the bacteria. *S.*Tm^{GFP} accumulates on the Z-layer and traverses the mucus in a few cases. (C) Time-lapse imaging of the tissue surface in image stack (B). *S.*Tm predominantly moves through areas with low fluorescence intensity. The tracks of the bacteria are shown in white. Fluorescent mucus is shown in red. (D) Quantification of the *S.*Tm swimming speed in the inner colonic mucus layer. The average *S.*Tm swimming speed during the traversal of the *RedMUC2*^{98trTg} mucus did not differ from the speed measured in the proximal colon of *villin-RFP* mice (compare with Fig. 4 B). The bars indicate the median and quartiles. (E) Quantification of the mCherry -MUC2 fluorescence at the location of swimming or trapped *S.*Tm from time-lapse microscopy data. Entrapped bacteria were preferentially located at sites with strong mCherry-MUC2 fluorescence. This could either be attributable to heterogeneous mucus densities or different adhesion properties between mucus of murine and human origin. Shown is the average fluorescence intensity beneath trapped *S.*Tm compared with swimming bacteria in the same image series. Each dot represents one time-lapse movie. Error bars delineate the mean ± SD. Statistics: Wilcoxon signed-rank test (non-parametric) testing whether the fluorescence ratio is different from 1.

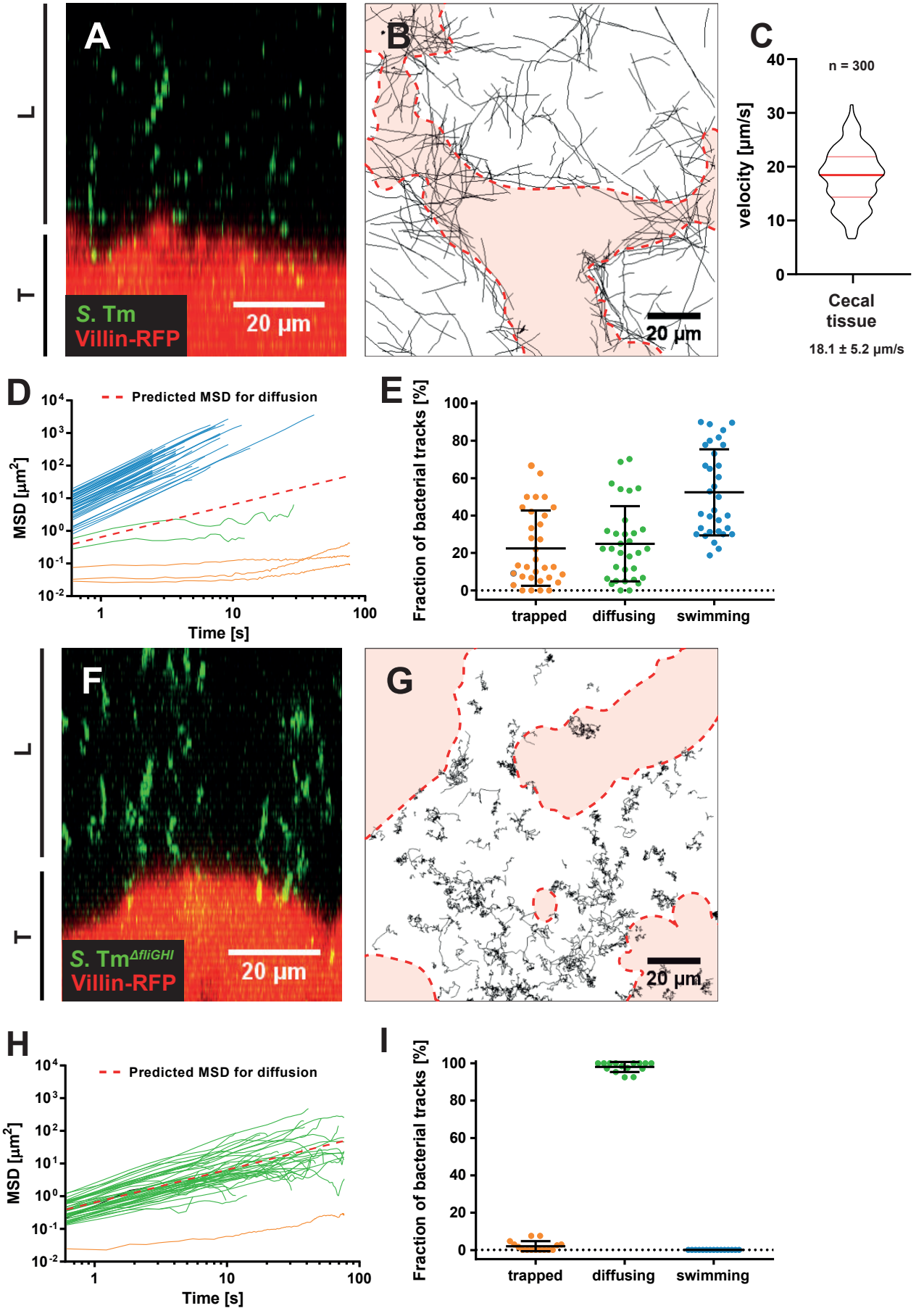
A
B
C
L
T
S. Tm
Villin-RFP
20 µm
n = 300
velocity [µm/s]
Cecal tissue
18.1 ± 5.2 µm/s
D
Predicted MSD for diffusion
MSD [µm²]
Time [s]
E
Fraction of bacterial tracks [%]
trapped
diffusing
swimming
F
G
S. TmΔfliGHI
H
I

Fig. S4, related to Fig. 5: The cecum tissue is easily accessible for *S.*Tm. (A - E) Cecal tissue samples were excised from untreated *villin-RFP* mice and mounted on a petri dish. After mounting, *S.*Tm^{GFP} was added onto the tissue and confocal image stacks were acquired. (A) Side-view of a confocal z-stack from the cecum after addition of *S.*Tm. Labels indicate the tissue (T) and the lumen / loose mucus (L). (B) Time-lapse imaging of the tissue surface in image stack (A). The tracks of the bacteria are shown in black. The red area marks the cecal tissue. See also Movie M7. (C) Swimming speed of actively moving *S.*Tm at the cecal tissue surface. Bars indicate the median and the quartiles. (D) Mean Squared Displacement (MSD) calculated from 50 random *S.*Tm tracks at the cecal tissue surface. The plot is color-coded for the motility phenotype of each track as in Fig. 1. (E) Trapped, diffusing and swimming *S.*Tm were quantified manually based on optical appearance of the tracks. Shown is the pooled data of three independent experiments. Each data point represents one image series. The error bars indicate the mean ± SD. (F - I) Cecal tissue samples were excised from untreated *villin-RFP* mice and mounted on a petri dish. After mounting, green fluorescent *S.*Tm$^{\Delta fliGHI}$ were added onto the tissue and confocal image stacks were acquired. (F) Side-view of a confocal z-stack from the cecum after addition of non-motile *S.*Tm$^{\Delta fliGHI}$. Labels indicate the tissue (T) and the lumen / loose mucus (L). (G) Time-lapse imaging of the tissue surface in (E). The tracks of the bacteria are shown in black. The red area marks the cecal tissue. (H) Mean Squared Displacement (MSD) calculated from 50 random *S.*Tm$^{\Delta fliGHI}$ tracks at the cecal tissue surface. The plot is color-coded for the motility phenotype of each track as in Fig. 1. (I) Trapped, diffusing and swimming *S.*Tm$^{\Delta fliGHI}$ were quantified manually based on optical appearance of the tracks. Shown is the pooled data of two independent experiments. Each data point represents one image series. The bars indicate the mean ± SD.

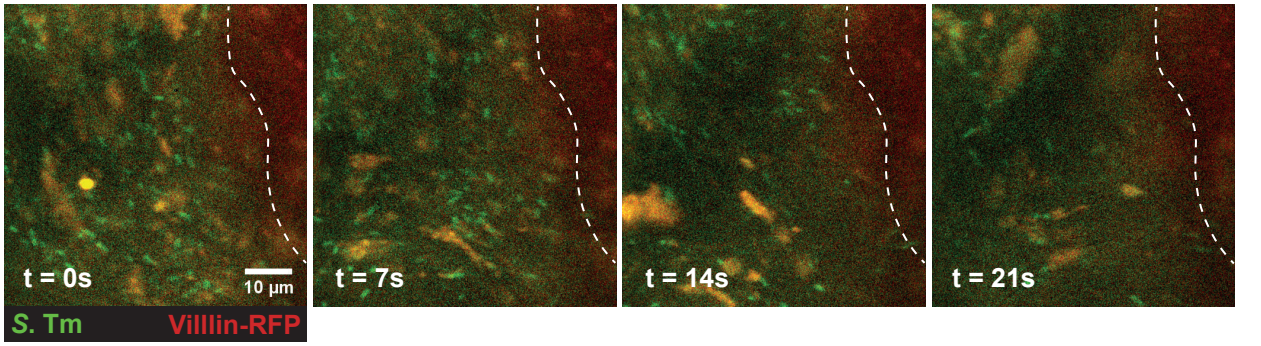
t = 0s
10 µm
t = 7s
t = 14s
t = 21s
S. Tm
Villlin-RFP

Fig. S5, related to Fig. 6: Light-induced heating of the samples leads to mixing of the intestinal content during intra-vital microscopy. *S.*Tm^{GFP} was injected into the cecal lumen of an anaesthetized *villin-RFP* mouse. *S.*Tm movement in the cecal lumen was tracked over time using two-photon microscopy. See also Movie M9. Fluorescent *S.*Tm^{GFP} are depicted in green. The border of the red fluorescent tissue is marked with the white dashed line. Auto-fluorescent food particles appear in orange. Thus, microscopy artefacts prevented more detailed analysis of the pathogen mucus interaction in the intact mouse gut.